UNIVERSITY OF CALIFORNIA
SANTA CRUZ

ELECTROMAGNETIC COMPATIBILITY AND RENEWABLE POWER FOR IMPLANTABLE NEUROSTIMULATORS

A dissertation submitted in partial satisfaction
of the requirements for the degree of

DOCTOR OF PHILOSOPHY

in

ELECTRICAL ENGINEERING

by

Oxana S. Pantchenko

June 2012

The Dissertation of Oxana S. Pantchenko
is approved:

Professor Michael Isaacson, Chair

Professor Ali Shakouri, co-Chair

Professor John Vesecky

Tyrus Miller
Vice Provost and
Dean of Graduate Studies

Table of Contents

List of Figures

List of Tables

Abstract

Electromagnetic Compatibility and Renewable Power for Implantable Neurostimulators
by

Oxana S. Pantchenko

Over the last decade, the number of implantable neurostimulator systems implanted in patients has been rapidly growing. Nearly 50,000 neurostimulators are implanted worldwide annually. The most common type of implantable neurostimulators is indicated for pain relief. At the same time, commercial use of other electromagnetic technologies is expanding, making electromagnetic interference neurostimulator function an issue of concern. Typically reported sources of neurostimulator EMI include: security systems, metal detectors, and wireless equipment. When near such sources, patients with implanted neurostimulators have reported adverse events such as shock, pain, and increased stimulation. The susceptibility of six active implantable neurostimulators with lead systems to an electromagnetic field generated by 22 radio frequency identification emitters was investigated. It was found that one implantable Neurostimulation system was inhibiting the stimulation pulse during low frequency exposure at close distances. This could potentially be due to induced electrical currents inside the implantable neurostimulator leads that are caused by magnetic field coupling from the low

frequency identification system. To systematically address the concerns posed by EMI, a test platform was developed to assess the interference from coupled magnetic fields on implantable neurostimulator systems. To measure interference, the output of one implantable neurostimulator, programmed for best therapy threshold settings was recorded, when in close proximity to an operating low frequency radio frequency emitter. The output of the same neurostimulator system programmed for best therapy threshold settings was also recorded without radio frequency interference. Using the Spatially Extended Nonlinear Node model, we compared the threshold factors of spinal cord fiber excitation for both recorded outputs. The electric current induced by the low frequency radio frequency emitter was not significant to have a noticeable effect on electrical stimulation.

The lifetime of any active neurostimulator system heavily depends on its battery. Current technology has been able to provide solutions to power up such devices for up to five years. In fact, the latest research in this area showed that, on average, batteries last only three years. When an implantable battery needs to be replaced, a surgical procedure is required during this process. In addition, the current available implantable batteries contain potentially hazardous materials to human bodies and if leaked could cause potentially lethal complications. A system was developed that demonstrates a proof of concept battery based on cascaded concentration cells that can currently deliver 2 μW of power, capable of powering small scale implantable devices such as pacemaker. Ideally, the system could replace or charge an existing battery based on concentration differences that already exist

within the human body. The system has several advantages over the current implantable batteries and other proposed technologies. The most important advantage is the use of flexible, biocompatible materials. Our system does not use toxic or nuclear materials. It does not depend on energy sources outside of the human body or body movement. It does not heat body tissue, or require a cosmetic disadvantage. It makes use of renewable energy sources within the body.

I'm dedicating this work to my wonderful mother, father, husband and the newborn son Andrew

Acknowledgment

I owe my deepest gratitude to my amazing advisors, Prof. Ali Shakouri and Prof. Michael Isaacson. I have received unlimited support and tremendous knowledge from Prof. Ali Shakouri and endless guidance from Prof. Michael Isaacson. Thank you for everything and much more!!!

In the last four years, I've been a part of Quantum Electronics and BioMedical Engineering research groups. It was an absolute pleasure to interact with each member on regular basis. I'm grateful to all past and present group members for their shared knowledge and expertise.

I would also like to extend my gratitude to my academic advisor, Carol Mullane for her great encouragement and advice during difficult times. I would also like to thank Carolyn Stevens for sharing her experience and providing great faculty support and Frances Ruiz-Wood for her assistance and unlimited guidance in purchasing and reimbursement processes.

Additionally, I would like to thank bels staff for their unlimited electronic part supply and fast poster printing, as well as, machineshop staff for their quick turnaround times and fantastic parts made from scratch.

Lastly, I would like to thank my east coast colleagues; Seth Seidman, Josh Guag, Victor Krauthamer, Alan M. Diamant, J. Patrick Reilly, Howard Bassen, Brian Beard, Karen Shelby, Isaac Chen and Curt Sponberg for their shared knowledge and experience and an opportunity to conduct research at the Science and Engineering Laboratories at the U.S. Food and Drug Administration.

Thank you to my family members and friends, without you this dissertation would have not been possible!!!

1. Introduction

It was around 15AD when a freed slave of Emperor Tiberius, who was suffering from painful gout, accidently stepped on an electric fish and felt a severe shock. From the occurrence of this event, his pain was much less felt. This is when the Emperor's physician, Scribonius, made a record to recommend the electric fish treatment for chronic pain [1]. Such remedy started being used for treating hemorrhoids, gout, depression, and epilepsy [2]. Seventeen hundred years later, Benjamin Franklin investigated after an event of muscle contraction cause by electric shock. At the beginning of 20th century, the first non-implantable electrical stimulator appeared on the market. It was told to cure pain, as well as, many other imaginable physical maladies. It was operating with an external battery [3]. In the 1960's typical electrical stimulators consisted of two parts, one passive and one active. The passive part, made of an electrode, was implanted inside the patient and was connected to an antenna. The active part was located outside of patient's body consisted of a similar type of antenna, control box and battery. It wasn't until 1981 that a fully implantable neurostimulator system was introduced by Medtronic [3]. Since then, the applications for implantable neurostimulation devices expanded requiring various implantation sites and electrode length though out the human body. As other technologies emerge on the market, the US Food and Drug Administration is closely watching adverse events of implantable neurostimulation devices. Some of the common adverse events

of the current commercially available neurostimulators include electromagnetic interference and battery failure.

In this dissertation, two specific areas of neurostimulation device research was explored. In Chapter 2.1., the electromagnetic compatibility of several commercially available neurostimulation devices to radio frequency identification systems is investigated. Additionally, the results of such investigation are presented and a systematic test protocol is discussed. In Chapter 2.2., magnetic field coupling and induced electric currents inside neurostimulator leads are investigated from a neurological point of view. Again, the results of such investigations are presented and a systematic test protocol is proposed. In Chapter 3, a renewable power source for implantable devices is introduced and developed. Several kinds of calculations and analysis are performed and presented.

2. Electromagnetic Compatibility of Implantable Medical Devices

2.1. Testing Electromagnetic Compatibility of Implantable Neurostimulators

2.1.1. Background

In the last several years, radio frequency identification (RFID) technology has become a popular choice for tracking people, animals, products and goods. This type of technology serves the same purpose as bar coding systems and magnetic strip systems, which is to provide identification. One advantage of RFID technology versus other types of technologies is the proximity for identification. Another advantage is the information stored in such systems can be programmed and reprogrammed, providing a robust way to store information. For example, bar code scanners (readers) need direct line of sight to identify barcodes. In magnetic strip technology, the magnetic strip cards have to be swiped through or very close to the reader to be identified. In RFID technology, RFID readers can be meters away from identification tags and still be able to identify them. This technology works by emitting and receiving radio and sub-radio frequency electromagnetic energy. Since RFID technology has gained popularity in many industries, an average person could get exposed to the emitted fields from RFID readers when using public transportation,

shopping at a grocery store, picking up a package at a postal service and driving through a toll booth [4, 5].

RFID technology is favored for certain uses due to its contactless transfer of data and storage capacity [4] and is quickly merging into health care and pharmaceutical industries. The United States Food and Drug Administration (FDA) is encouraging use of a state-of-the-art technology, such as RFID, that tags product packaging electronically because it allows manufacturers and distributors to precisely track drug products through the supply chain [6]. A number of hospitals are adopting RFID technology to help locate doctors, nurses, patients and expensive medical equipment [7] and RFID systems have been deployed for tracking items used in the surgical suites, such as, sponges, needles and surgical instruments [8]. Other RFID systems have capability to monitor temperature and are being utilized in pharmaceutical industry for temperature compliance purposes [7]. Overall, RFID systems offer a variety of benefits that include fast transactions, real time tracking, contactless data transfer, large storage capacity and continuous temperature monitoring. Some claim that RFID technology can change the delivery of patient care [9].

Similarly to other sources of electromagnetic energy, the emissions from RFID systems can be a source for electromagnetic interference (EMI) with medical devices. The potential risks of EMI with RFID emissions can be illustrated by the study conducted by van der Togt *et. al.* that reported potentially hazardous incidents in

critical care medical equipment caused by RFID system emissions. The hazardous incidents were events that could have a direct physical influence on a patient by unintended change in equipment function [10]. In a more recent study, Seidman *et. al.* investigated electromagnetic compatibility (EMC) between RFID and implantable pacemakers and implantable cardioverter defibrillators (ICDs). The pacemakers and ICDs were exposed to RFID readers of 134 kHz, 13.56 MHz, and 915 MHz carrier frequencies. The results showed that during 134 kHz RFID reader emissions, a reaction was observed for 67% of all pacemaker tests and 47% of all ICD tests. Observed reactions by implantable pacemakers and ICDs included pacing inhibition, inappropriate pacing, noise reversion mode, changed pacing rates, inappropriate delivery of antitachycardia pacing, inappropriate delivery of high voltage shocks and a change in device programming [11].

Active implantable neurostimulator devices are similar to pacemakers and ICDs that potentially could be susceptible to electromagnetic interference from RFID emissions. Unlike implantable pacemakers and ICDs, FDA approved implantable neurostimulators do not have sensing capability and operate as open loop systems with the patient to close the loop. Implantable pacemakers and ICDs include cardiac sensing capabilities in order to sense electrophysiological signals that might make these devices more sensitive to external low frequency RF signals. Due to their sensing capabilities, it is hypothesized that pacemakers and ICDs might be more likely to misinterpret certain external RF emissions as an electrophysiological signal.

In recent years, the FDA has received a number of reports suggesting EMI with deep brain stimulators from various electromagnetic sources [12]. Kainz *et. al.* described various sources of EMI, which included a report from a patient with an implantable spinal cord stimulator who received an electric shock while walking near an article surveillance device [13]. Several incident reports and published literature culminated in the 1998, the FDA advisory issued a letter to cardiologists, cardiovascular surgeons, emergency physicians, neurologists and neuro surgeons warning about the operation of certain medical devices, including spinal cord stimulators, may be affected by the electromagnetic fields produced by anti-theft systems and metal detectors [14]. The present study extends the investigation of potential EMI effects on implantable neurostimulators with emissions from RFID emitters.

2.1.2 Methods

2.1.2.1 Materials

Six active implantable neurostimulators were analyzed for EMC with 22 RFID emitters. Each implantable neurostimulator was approved by the FDA for intended uses that include: epilepsy, depression, incontinence, Parkinsonian tremor and pain relief. All six implantable neurostimulators consisted of implantable pulse generators (IPG) and implantable leads with platinum/iridium electrodes. All implantable neurostimulators were open loop systems where the physician and patient program

and control the stimulation. During testing exposures to the emissions from the RFID, all neurostimulators were carefully monitored for effects of EMI, such as change in stimulating parameters, changes in programmable settings, change in operating mode, false alarms, initiation of any unintended operation and changes in programmable parameter settings. Due to the nature of this study and the cooperative agreement set up between multiple neurostimulator manufacturers and the FDA, the name and the model of each implantable neurostimulator will be withheld and device under test (DUT) number assigned. Table 1 lists additional characteristics of the tested implantable neurostimulators.

Table 1: Characteristics of Implantable Neurostimulators

DUT	Indication	Stimulation Modality	Longest Lead Length Tested (cm) [a]	Number of leads connected to the neurostimulator
1	Epilepsy and depression	Bi-polar	43	1
2	Epilepsy and depression	Bi-polar	43	1
3	Incontinence	Bi-polar	41	1
4	Parkinsonian tremor	Bi-polar	135	2
5	Pain relief	Bi-polar	75	2
6	Pain relief	Bi-polar	135	2

[a] In the case of the neurostimulator system tested with lead extensions, the longest length reported includes the length of the extension lead.

Twenty two RFID emitters were used in EMC testing with implantable neurostimulators. LF and HF systems primarily emit magnetic fields while UHF systems primarily emit electric fields. Table 2 shows the appropriate RF and physical characteristics of all 22 RFID emitters. For Emitters 1-5, the measurements were made with magnetic field probe Model 1709.001 (Electric Research and Management) and for Emitters 6-13 the measurement were made with magnetic field probe, Model H3DV7 (SPEAG). For Emitters 14-16 and 21, 22, the measurements were made with electric field probe, Model SRM-3000 (NARDA) and for Emitters 17-20, the measurement was made with electric field probe, Model HI-6105 (ETS-Lindgren). In all measurements, probes were connected to a robotic arm to maneuver along RFID antennas. The probes were aligned perpendicularly to RFID antennas and measured field strength along the flat surface of each antenna.

Table 2: Characteristics of RFID emitters.

Emitter	Emitter/ Reader Antenna Dimensions (cm)	Standard Used	Emitter Carrier Frequency (MHz)	Max. H-field (A m^{-1}) at 2.5 cm [a]	Max. E-field (RMS) (V m^{-1}) at 10 cm
1	Rectangular Loop 114 x 66 x 6.3	—	0.125	13.3	—
2	Rectangular Loop 3.5 x 4.5 x 0.5	—	0.125	1.2	—
3	Rectangular Loop 20 x 20 x 2.5	ISO 11785	0.134	269.0	—
4	Rectangular Loop 85 x 50 x 5	—	0.134	68.0	—
5	Rectangular Loop 85 x 50 x 5	ISO 11785	0.134	162.0	—
6	Rectangular Loop 31 x 31 x 2.8	ISO 18000-3 mode 1	13.56	4.6	—
7	Rectangular Loop 20 x 20 x 0.8	ISO 18000-3 mode 1	13.56	4.9	—
8	Rectangular Loop 31 x 31 x 2.8	—	13.56	8.6	—
9	Rectangular Loop 31 x 31 x 2.8	ISO 18000-3 mode 1	13.56	8.7	—
10	Rectangular Loop 31 x 31 x 2.8	ISO 18000-3 mode 1	13.56	8.8	—
11	Handheld 19 x 11 x7.8	ISO 18000-3 mode 1	13.56	7.8	—
12	Patch 2.3 x 2.5 x 0.1	ISO 1443A, 1443B, 15693, 18000-3	13.56	2.4	—
13	Patch 21 x 32 x 1.2	ISO 18000-3 Mode 2	13.56	18.6	—
14	Patch 15.7 x 5.5 x 3	ISO 18000-7	433	—	0.4
15	Stick length 19.8 x diameter 1.4	—	433	—	——
16	Patch 38 x 36.5 x 1.5	—	433	—	——
17	Patch 31 x 31 x 4.8	ISO 18000-6B	915	—	79.3
18	Patch 48.5 x 31 x 5	ISO 18000-6B	915	—	36.2
19	Patch 21 x 21 x 3.5	ISO 18000-6	915	—	97.3
20	Patch 22.5 x 21 x 5	ISO 18000-6C	915	—	69.8
21	Stick length 10.5 diameter 0.9	—	2450	—	0.02
22	Stick length 11 diameter 0.8	—	2450	—	1.0

[a] Maximum H-field strength at 2.5 cm for Emitters 1-5 was measured using magnetic probe Model 1709.001, Electric Research and Management. For Emitters 6 – 13, the maximum H-field strength was measured using magnetic probe, Model H3DV7, Speag. For Emitters 14-16 and 21, 22, the maximum E-field was measured using E-field probe, Model SRM-3000, NARDA. Measured electric field of Emitters 15 and 16 was below the sensitivity level of the probe. For Emitters 17-20, the maximum E-field was measured using E-field probe, Model HI-6105, ETS-Lindgren.

In general, RFID systems consisted of interrogators (active emitters) and transponders (active and passive emitters). The interrogators, sometimes called readers, were designed to read information from transponders. RFID transponders are referred to as tags are either active or passive devices that transmit their information to reader. For this study, the term RFID emitter describes the 21 RFID readers and one active RFID tag. Five of the RFID emitters operated using a carrier frequency between 125 and 135 kHz and are typically used for access control for animals and people. Twelve RFID emitters operate using a carrier frequency of 13.56 MHz that is typically used in libraries, passports, payment emitters and smart cards. Three of the tested RFID emitters operated using a carrier frequency of 433MHz that are typically used for asset tracking. One of the tested RFID emitters operated at a carrier frequency of 915 MHz that are typically used in retail and military supply chain tracking. Lastly, one RFID emitter operated at a carrier frequency of 2.45GHz typically limited to niche uses [11]. Due to the nature of this study and the cooperative agreement set up between multiple RFID manufacturers and the FDA, the name and the model of each RFID emitter will be withheld and RFID number assigned.

2.1.2.2. Test Method

The test method for the present study originated from ANSI/AAMI/ISO 14708-3:2008 American National Standard for Implants for Surgery – Active implantable Medical Devices – Part 3: Implantable Neurostimulators [15]. The standard was

recognized for developing *in vitro* EMC test protocols for implantable neurostimulators using a torso simulator tank made of a polyethylene plastic box (58.5 cm x 42.5 cm x 15.2 cm) filled with 0.27 S/m saline solution to represent static electrical properties of the body. A non-conductive, non-metallic plastic grid cut from a fluorescent light fixture cover was used as a support grid for the neurostimulator device and the lead system. The grid was suspended with plastic legs inside the saline solution that allows adjustable elevation within the saline. The DUT was submerged 5 mm deep into the saline bath parallel to the surface. Figure 1 demonstrates top view of the test set-up.

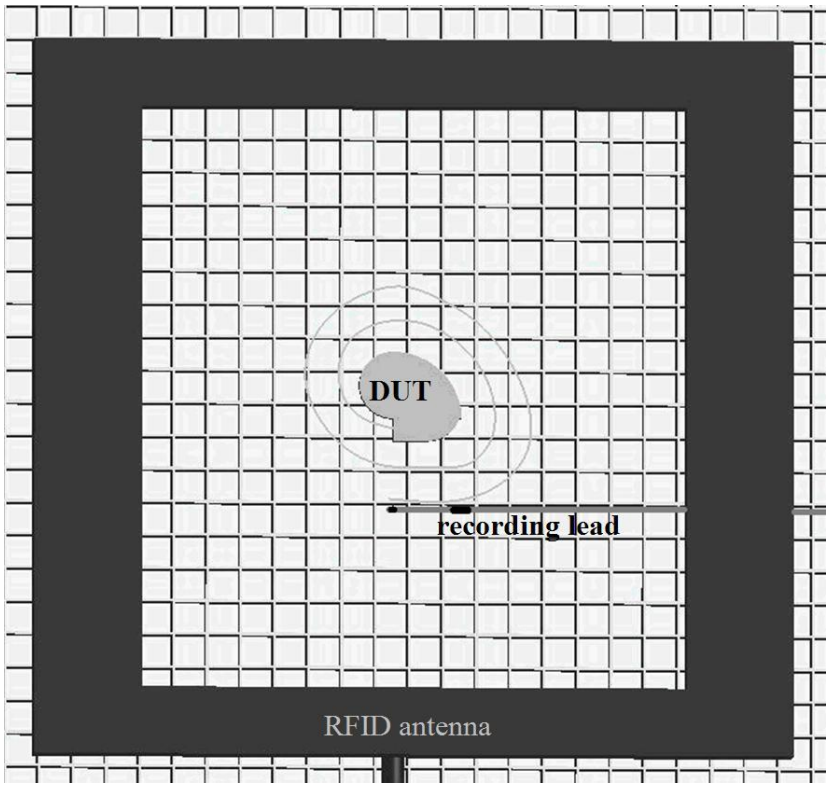

Figure 1: Overall configuration: Configuration of RFID antenna, implantable neurostimulator system and pick-up lead. The implantable neurostimulator system and the pick-up lead were positioned in the same z- plane. The RFID antenna was parallel to the neurostimulator system.

Four out of the six implantable neurostimulators use voltage based stimulation and were programmed to generate pulses of electrical potential amplitude (4.2-5.2V), frequency (2-3Hz), pulse width (210-500 usec). The other two implantable neurostimulators use a current based stimulation and were programmed to output pulses of electrical current amplitude (1.75 mA), frequency (2 Hz) and pulse width (500 usec). Overall, the output amplitude of the devices was set to the half of their peak maximum amplitude, the maximum pulse width and the smallest programmable frequency. These parameters were chosen to allow the greatest range of observation for detecting disruptions or changes to the DUT output that could be attributed to RFID emissions exposure.

In the cases where a neurostimulator system had more than two stimulating electrodes per lead system, the electrodes that were furthest apart were activated for consistency among all tested systems. If a neurostimulator system had an option of using bi-polar or unipolar setting, the bi-polar setting was chosen for consistency among all tested neurostimulator systems. If a neurostimulator system had an option of using different lead lengths, the leads of maximum lengths were chosen due to the expectation that this would capture a larger portion of the RFID emissions and allow for greater coupling to the electromagnetic fields into the DUT. A bi-polar pacemaker lead connected to a digital oscilloscope was placed in the saline bath within a few

millimeters from the neurostimulator electrodes to record the output pulses from the DUT.

A non-conductive, non-metallic fiberglass robotic arm was used to maneuver each RFID emitter parallel to the open surface of the stimulator system. Starting at 60 cm vertical separation distance from the DUT, the robotic arm moved the RFID emitter closer to the submerged DUT in increments of 5 cm. The closest separation distance between the DUT and the RFID emitter was 2.5 cm. Figure 2 shows the H-field strengths at perpendicular distances apart from the RFID emitter antennas for Emitters 3 and 5.

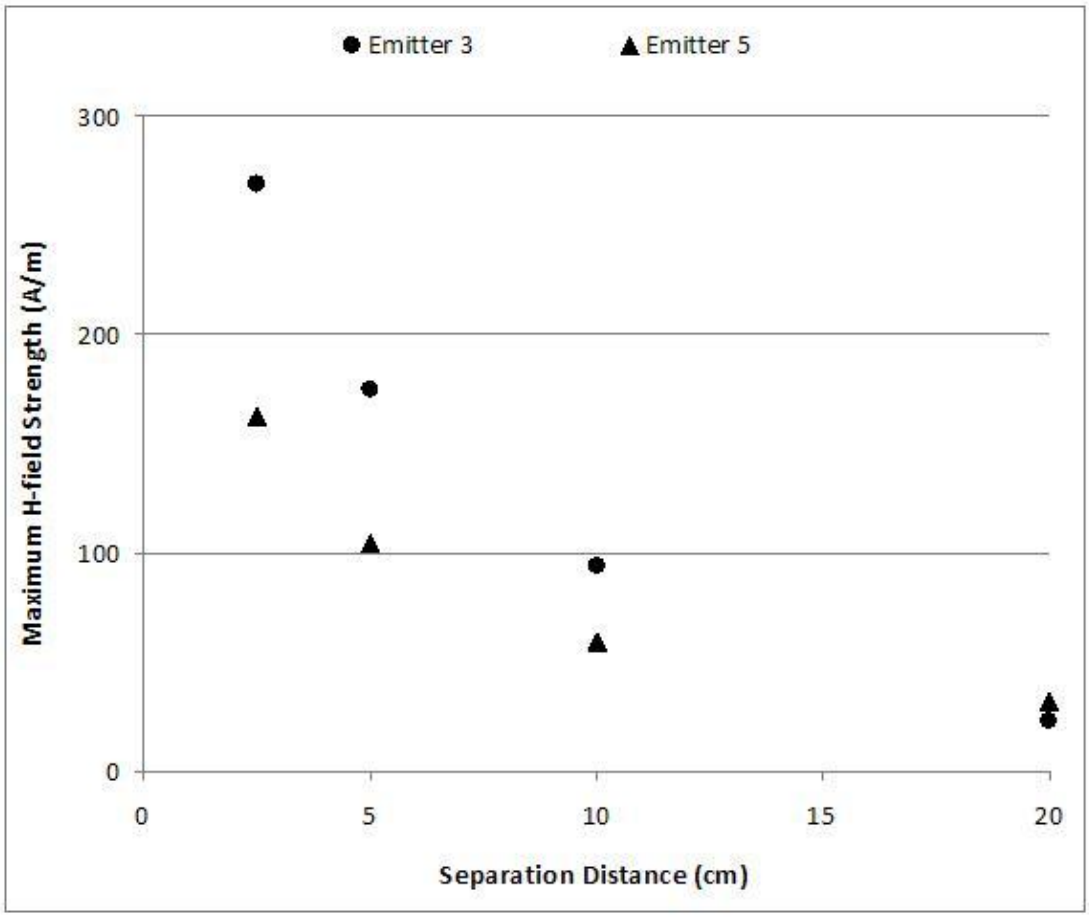

Figure 2: H-field measurements: Measured maximum H-field strength at 2.5, 5, 10 and 20 cm away from the antenna for Emitters 3 and 5.

2.1.2.3. Test Procedure

Each DUT was configured with IPG placed in the middle of the support grid and the leads and electrodes wrapped in a spiral around the IPG as specified in the ANSI/AAMI/ISO 14708-3:2008 Standard [15]. For consistency, each lead was wrapped twice around the IPG with the distance between the center of IPG to the furthest electrode held equal to the following,

$$\text{distance} = \sqrt{\left(\left(0.09 * \text{lead length}^{2} \right) / \pi \right)}$$

The lead system was secured in place with non-conductive cotton thread and the conductivity of the saline bath measured and if needed corrected to 0.27 S/m. The DUT with the support grid was submerged into the saline tank to a depth of 5 mm. The bi-polar recording lead was then placed into the saline bath within millimeters away from DUT. The DUT was programmed and activated and output of the IPG was verified on the oscilloscope. For each measurement, the robotic arm was raised 60 cm away from DUT then RFID emitter antenna was placed on top of the robotic arm and centered directly over the DUT. The RFID emitter was turned on and verified for proper operation. The robotic arm with RFID antenna were lowered in 5 cm increments until the separation distance of 5 cm was reached. The robotic arm was then additionally lowered to 2.5 cm above the DUT for worst case test. Thirteen distances of separation were verified for exposures. The behavior of the neurostimulator under each test condition was observed for 15 seconds and recorded. Any change in output signal was noted as an effect. The same test procedure was repeated for each of the 22 RFID emitters resulting in the total of 1716 observed tests (6 neurostimulator systems x 22 RFID emitters x 13 tested distances).

2.1.3. Results

EMC was investigated between six implantable neurostimulators and 22 RFID emitters at 13 distances of separation. A total of 1716 tests were administered. Six tested implantable neurostimulators did not show any effects when exposed to RFID emitters with 125 kHz, 13.56 MHz, 433 MHz, 915 MHz and 2.45 GHz carrier

frequencies and continued their normal mode of operation before, during and after exposures.

Seven effects were observed from exposures between RFID carrier frequency of 134 kHz and DUT 3. The output of DUT 3 with lead length of 41 cm was inhibited by Emitter 3, with a 134 kHz carrier frequency, at separation distances of 2.5, 5 and 10 cm. The output of the same implantable neurostimulator with the same lead length was also inhibited by Emitter 5, with a carrier frequency of 134 kHz, at separation distances of 2.5, 5, 10 cm and also showed inconsistent pulsing rate at a separation distance of 15 cm. All effects were transient occurring only during exposure.

In order to investigate EMC of DUT 3 further, additional tests were performed. The neurostimulator was tested with shorter lead lengths of 28 cm and 33cm. The DUT 3 with each lead length was exposed to Emitters 3 and 5 in the same way as described in the Test Method and Test Procedure sections of this paper. The following effects were observed,

- DUT 3, lead length of 33 cm exposed to Emitter 3
    - the output was inhibited at 2.5, 5, and 10 cm of separation distance
- DUT 3, lead length of 33 cm exposed to Emitter 5
    - the output was inhibited at 2.5 and 5 cm of separation distance
- DUT 3, lead length of 28 cm exposed to Emitter 3
    - inconsistent pulsing rate at a separation distance of 10 cm

    - the output was inhibited at 2.5 and 5 cm of separation distance
- DUT 3, lead length of 28 cm exposed to Emitter 5
    - the output was inhibited at 2.5 and 5 cm of separation distance

All DUT effects occurred during and lasted throughout the duration of the particular separation distance and exposure from RFID emitters. Additionally, Figure 2 shows measured maximum H-field strength at distances of interest.

2.1.4. Discussion

Effects from EMI were observed when DUT 3 was exposed to the electromagnetic fields from RFID emitters operating at the 134 kHz carrier frequency. Two major distinctions between 134 kHz RFID emitters and emitters of higher frequencies are their carrier frequency and the antenna type. Close to the emitter antennas, also known as the "near field" region, low frequency antennas emit primarily magnetic fields. This is the case for tested 134 kHz RFID tested emitters. Emitters 3 and 5 that caused EMI have magnetic field intensities that are at or above 162 A/m at 2.5 cm away from antenna. From theory, in the near field region, the strength of the magnetic field decreases with the cube of a distance [4]. This explains why the same types of effects did not occur at greater distances of separation.

More effects on the DUT3 were observed at larger distances of separation with Emitter 5 that has H-field strength less than the one of Emitter 3 at 2.5 cm. This could be due to the effects that larger antennas have. It is true that for RFID antennas with

larger dimensions, the field strength decreases more slowly than for antennas of smaller dimensions. Fig. 2 demonstrates the principal of field strength curve vs. distance of separation. For example, Emitter 3 has higher field strength at the separation distance of 10 cm; however, Emitter 5 has higher field strength at 20 cm of separation distance. This could explain observed effects seen at 15 cm with Emitter 5 and not with Emitter 3.

Additional testing of DUT 3 with lead lengths of 33 cm and 28 cm and Emitters 3 and 5 indicate that the lead length is related to a number of effects. DUT 3 with lead length of 41 cm, seven effects were observed with the maximum distance of separation of 15 cm. DUT 3 with lead length of 28 cm, five effects were observed with maximum distance of separation of 10 cm, therefore the number of observed effects increases with increased lead length. This effect could be due to the induced current coupling into the leads and the neurostimulator system. Induced current is proportional to the area formed by the lead; the larger the area, the greater the electric current in the system.

One possible explanation for the effects seen with DUT 3 and Emitters 3 and 5 is related to the telemetry frequency (frequency used to communicate between the neurostimulator and the programmer) and the neurostimulator control design. The telemetry frequency of DUT 3 is very near carrier frequency of Emitters 3 and 5. Additionally, DUT 3 is designed to inhibit stimulation during telemetry process. This

period lasts between 42 – 84 ms depending on the number of ones and zeros in the data. If the RFID reader emits a pulse every 42 ms (or quicker) than we would expect complete inhibition. Depending on timing RFID readers that pulse less frequently could partially inhibit the neurostimulator.

The clinical significance of the effects was analyzed by a clinician at the FDA. Two scenarios were considered, short term exposure and extended period of time exposure from RFID emitters. Short term exposure is equivalent to a patient walking through or by RFID emitter. Short term exposure could cause temporary effects, in this case only minor changes or no changes at all would likely be noted by the patient. Extended period of time exposures are equivalent to a patient spending long periods of time near an RFID emitter. In this case, long term exposure could cause long term effects that are clinically significant and therefore making it likely that the patient's original symptoms of incontinence to return.

2.1.5. Limitations

There are several limitations of this study that should be discussed. The study was conducted on a phantom filled with saline solution representing average conductivity of a human body at all frequencies of interest. During the study, the RFID antennas were centered over implantable neurostimulator systems, which might not represent the worst case scenario for square or rectangular antennas since the maximum field

strength is at the corners. Also, the configuration of implantable pulse generator and the lead system was a generalization across these devices taken from referenced standard [15] rather than a strict adherence to the way each device would likely be implanted. This configuration was chosen because it seems close to the worst case scenario for potentially inducing electromagnetic interference and maximizes the area and number of loops made by the lead system. Another important limitation of this study is the operation of RFID reader without RFID tag. In our study, we used RFID tags to verify proper operation of RFID emitters prior to testing and we did not use RFID tags during dwell time of each test. The presence of an RFID tag could affect the reader's modulation. It is also important to mention that few of our tested implantable neurostimulator systems had an option of unipolar stimulation. As we mentioned in Test Method section, we chose a bi-polar stimulation option for consistency purposes, since all of our neurostimulators offered such option. The unipolar stimulation option was not tested which defines anther limitation of this study.

2.1.6. Conclusion

In this study, EMC was investigated among six implantable neurostimulators and 22 RFID emitters. Most of the DUT implantable neurostimulators were unaffected by the RFID emissions. However, DUT 3 showed repeatable effects that included output inhibition and inconsistent pulsing rate from exposure to 2 different 134 kHz RFID emitters at separation distances from 2.5 cm up to 15 cm. The present study seems

generally consistent with a previously published study of active implantable devices that showed that EMI is most common for certain medical devices during exposure to 134 kHz frequency RFID emitters [13]. Manufacturers of active implantable devices need to be aware of the potential and risk of EMI from RFID emitters and design and their medical devices appropriately. Additionally, RFID industry should take into account the potential effects on active implantable medical devices when designing systems, configuring, and locating installation of their systems. Moreover, patients and physicians should all be aware of the possibility of adverse effects of implantable neurostimulators from RFID emitters. In the future, our goal is to increase the number and variety of tested implantable neurostimulators and simulate RFID emitters to decrease testing time.

2.2. Analysis of Induced Electrical Currents from Magnetic Field Coupling Inside Implantable Neurostimulator Lead

2.2.1. Introduction

In the previous chapter, we investigated the EMC of six implantable neurostimulators and 22 RFID emitters. We found effects of inhibition of one implantable neurostimulator system indicated for incontinence when close to two low frequency RFID emitters. The effects were determined to be clinically significant only if they occurred for extended periods of time. There were no observed effects on the other 5 implantable neurostimulators or during exposures from other RFID emitters [16]. Additional publication reported that magnetic fields can turn the stimulation on or off and varying magnetic fields can momentarily inhibit telemetry [17].

A previously published study has also shown that magnetic resonance systems are capable of generating strong magnetic fields that could potentially cause nerve stimulation. The induced fields inside the patients with implantable leads are much larger than induced fields inside patients with no implantable systems [18]. To address the concerns posed by coupling of electromagnetic fields from RFID emitters, we developed a test protocol to assess the interference from coupled magnetic fields on implantable neurostimulator systems.

2.2.2. Background Theory

In the 1830s, Michael Faraday proposed a hypothesis that a magnetic field could produce an electric current in a wire. After 10 years of experiments, Michael Faraday and Joseph Henry independently discovered that magnetic fields can produce an electric current in a closed loop, but only if magnetic flux linking the surface area of the loop changes with time. This type of process was named electromagnetic induction. The electric current can be generated under any one of the three conditions:

1. A stationary loop in a time varying magnetic field,
2. A moving loop with a time varying area in a static magnetic field, or
3. A moving loop in a time varying magnetic field [19].

One hundred and eighty years later, the same theory still holds. This relation is now known as Faraday's law of induction.

In our work, we chose to focus on the first example of a stationary loop in a time varying magnetic field since it represents the worst case scenario of magnetic fields coupling at the minimum separation distance. In our study, the time varying magnetic field is generated by the RFID emitter and a stationary loop is formed by the implantable neurostimulator leads.

In the case of a single turn, conducting circular loop with surface area A in a time varying magnetic field B(t), the electrical potential difference between the ends of leads is defined as,

$$V = \int \partial/\partial t\, B \cdot dA$$

where,

V: electrical potential difference (V)

$\partial/\partial t$ B: rate of change of the magnetic field (T/s)

A: surface area of the enclosed loop (m^2) [19]

2.2.3. Methods

2.2.3.1. Probe for Measuring Electrical Potential Difference

A probe was designed for measuring the electrical potential difference between two contacts of the pulse generator. The probe was made of solid conductor copper wires of American Wire Gauge 26 and a "U" shaped custom modified connector. Two pieces of copper wire were twisted and soldered to the "U" shaped custom modified connector. The connector's bare tips were separated by 5 mm and were approximately 5 mm long. The dimensions of this probe were defined by the design of the implantable neurostimulator system. The probe was designed to make contact with a set of screws that secure leads inside the pulse generator can. Figure 3

demonstrates such set up. The proximal end of the probe was connected to 1 Mega Ohm input impedance oscilloscope. The probe was oriented in a straight line parallel to the B field generated by the RFID antenna and perpendicular to the neurostimulator leads.

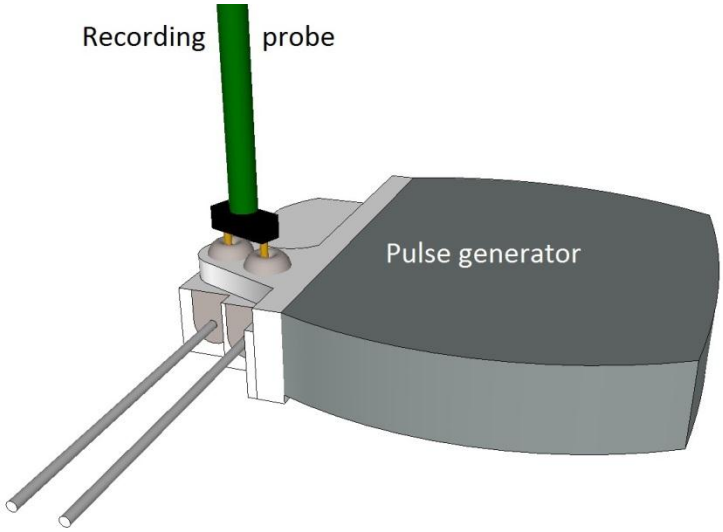

Figure 3: Recording probe and pulse generator with leads attached.

2.2.3.2. RFID Emitter

A commercially available RFID system was used for exposing the implantable neurostimulator system to magnetic fields. The system operated using International Organization for Standardization 11785 Standard. The carrier frequency was 134.2 kHz, which is considered low frequency, or LF RFID. Typically, systems with low carrier frequency are used in access control of animals and people [11]. The maximum magnetic field strength was measured to be 269 A/m at 2.5 cm away from the RFID antenna. The pulse repetition rate of this system is 10.7 Hz. The RFID

reader antenna dimensions are 20 cm x 20 cm x 2.5 cm. The highest magnetic field measured at close distances was near the corners.

2.2.3.3. Implantable Neurostimulator System

A commercially available implantable neurostimulator system was analyzed for coupling of electromagnetic fields. This system was previously approved by the FDA for intended use of pain relief. The system consisted of an implantable pulse generator and two implantable leads with platinum/iridium electrodes. Each lead was measured to be 75 cm long with 8 electrode contacts. The system operated as an open loop system and did not require a physiological signal for activation. The unique design of the pulse generator, that enabled us to record from the electrodes, allowed us to perform the tests without modifying the pulse generator or leads.

2.2.3.4. Patient Simulating Tank

We used a commercially available phantom ELI4, SPEAG. The phantom was made from vinylester, glass fiber reinforced material which is capable of holding up to 30 liters of fluid. The inside of the phantom has oval shape of 40 cm x 60 cm with the 2 mm bottom plate. The phantom was filled with saline solution of electrical conductivity that represents electrical properties of the body [20].

2.2.3.5. SENN Model

The Spatially Extended Nonlinear Node (SENN) model was developed by J. Patrick Reilly and Alan M. Diamant and recently published in Electrostimulation; Theory, Applications, and Computational Model for modeling various nerve and muscle

fibers[21]. The SENN model is based on a program developed by Donald McNeal in 1976. Reilly and Diamant have successfully employed this model in studying excitable tissue reactions to applied electrical forces. The SENN model accounts for temporal and spatial variations of electrical current in spinal cord fiber which includes variations in stimulus wave shape, duration, repetition pattern, magnitude, means of delivery at location of electrodes on the body, electrode size and biological and physiological factors. This model was previously used in analyzing medical applications of electro-stimulation, electric shock, exposure limits to patients in medical applications, electromagnetic safety standards and human reactions to electric weapons [21]. We implemented this model in analyzing coupling of electromagnetic fields when in close proximity to RFID emitters. The SENN model source code, supporting files, sample executable for PC and Mac platforms and a startup guide are available as free downloads at http://www.artechhouse.com/static/reslib/reilly/reilly.html.

2.2.3.6. Procedure

A non-conductive, non-metallic plastic grid was used as a support grid for the neurostimulator device and the lead system. The height of the grid was 7.7 mm. The plastic grid with the neurostimulator system attached was placed inside the patient simulation tank at the bottom. The tank was filled with 5280 µS/cm (0.528 S/m) conductivity saline to the top surface of the neurostimulator pulse generator. The conductivity value was selected to match reported 561 Ohm resistance [22] between

electrodes which were 6mm apart. The holes in the grid filled with the surrounding saline. Figures 4 and 5 demonstrate top and side views of the experimental set up.

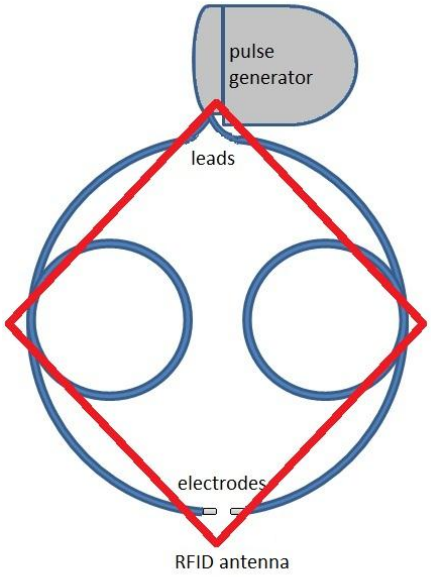

Figure 4: Implantable Neurostimulator System configuration. Top View. Each neurostimulator lead is 75 cm long, forming circular loops along RFID antenna (not shown). Assume the neuron submerged and is oriented perpendicular to the electrodes.

The neurostimulator system was configured so that the leads outline the RFID antenna and the extra length was looped around the outline of the corners of the antenna (Figure 4). The magnetic field around the corners of the antenna was previously recorded to generate the highest magnetic field strengths. This layout represents the worst case scenario for coupling electromagnetic fields into implantable leads. The worst case scenario layout was also verified experimentally. The neurostimulator system was programmed to measure the output impedance between most distal electrodes of each lead. At the separation distance between edges of electrodes of 6 mm and saline conductivity of 0.5280 S/m, the measured

impedance was 561 Ohms. This impedance value was within reported values for spinal cord stimulators with dual lead configuration of 562 ±389 Ohms [18].

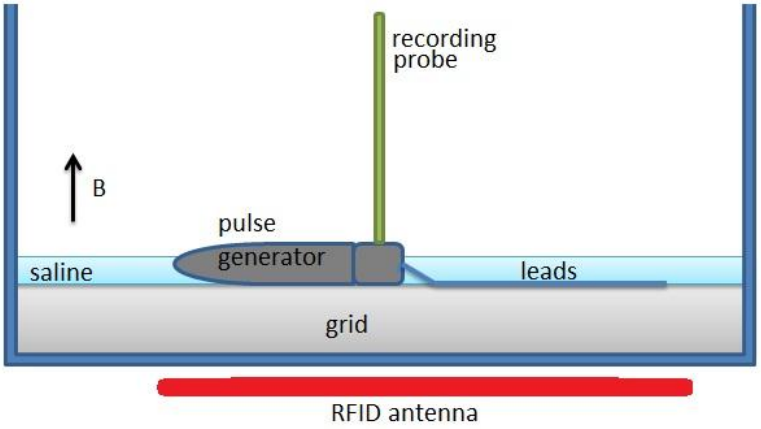

Figure 5: Implantable neurostimulator system configuration inside patient simulation tank with RFID antenna shown underneath the tank. Side View. The neuron is submerged 1.5 mm and is oriented perpendicular to the electrodes.

Neurostimulator parameters were chosen from a recent study that reported electric parameters optimized for spinal cord stimulation with conventional non-rechargeable neurostimulator systems, with a sample size of 73 systems. The average reported parameters for best therapy were; amplitude of 5.3 mA, pulse width of 300 µsec and pulse repetition of 100Hz (10msec) [22]. Since our implantable neurostimulator system was a voltage controlled system, we calculated 5.3 mA (through 561 Ohms impedance) to be 3V. We programmed the neurostimulator system to output a waveform of 3V amplitude, 300 µsec pulse width and 100Hz repetition rate.

Next, we connected our recording probe to the pulse generator. Using the oscilloscope, we verified programmed parameters and recorded the waveform. The same procedure was then performed three times to show repeatability.

We placed the RFID antenna underneath the saline-filled neurostimulator tank. The antenna was oriented parallel to the loop formed by the neurostimulator system's leads and perpendicular to the recording probe. Figure 5 demonstrates the side view of the layout. While the neurostimulator system was on, we turned on the RFID emitter. On the oscilloscope, we measured and recorded the output waveform which contained the waveform generated by the neurostimulator system and also the induced voltage coupled into the implantable neurostimulator leads. The same procedure was then performed three times to show repeatability.

The recorded data was then corrected for direct current (DC) coupling, possibly causing an offset that was not balanced out. This particular type of offset is considered to be caused by the recording set of instruments. The offset was determined by averaging a non-signal portion of the data and the bias was subtracted from all sample values [21].

The SENN model was then used to analyze corrected data to compile threshold factors for excitation of spinal cord fiber. The SENN model required a set of temporal and spatial parameters. We obtained spinal cord fiber standard parameters for

recruitment of dorsal column fibers in spinal cord stimulation from previously published work by Struijk *et. al.* [23]. Table 3 demonstrates the parameters in further detail. For spatial parameters, we considered the worst case scenario (the shortest distance between electrode and the nerve fiber) along with optimum electrode geometry published by Holsheimer and Wesselink [24]. Table 4 defines spatial parameters in further details.

Table 3: Spinal Cord Fiber Standard Parameters for Recruitment of Dorsal Column Fibers in Spinal Cord Stimulation [20]

Parameters	Values
diameter of main fiber	6 µm
nodal length	1.5 µm
intra axonal resistivity	0.7 Ohm m
medium resistivity	0.58 Ohm m
membrane conductivity	1280 Ohm $^{-1}$m $^{-2}$
membrane capacitance per unit area	0.02 F m $^{-2}$

Table 4: Spatial Parameters in Spinal Cord Stimulation

Symbol	Parameters	Values (cm)
Xc	x-coordinate of cathodic electrode	0.0
Yc	y- coordinate of cathodic electrode	0.15^{20}
Xa	x- coordinate of anodic electrode	0.6
Ya	y-coordinate of anodic electrode	0.15^{20}
$Wire_{L}$	wire electrode length	0.85
FS	spatial field source	wire electrodes
S	electrode environment	electrodes on surface

2.2.4. Results

We recorded two types of output waveforms from the implantable neurostimulator system. The first type of waveform contained only voltage signals from the implantable neurostimulator system. The second type of waveform contained voltage signals generated by the implantable neurostimulator and induced voltage caused by EMI from the RFID emitter. Figures 6 and 7 show the recorded waveforms respectively.

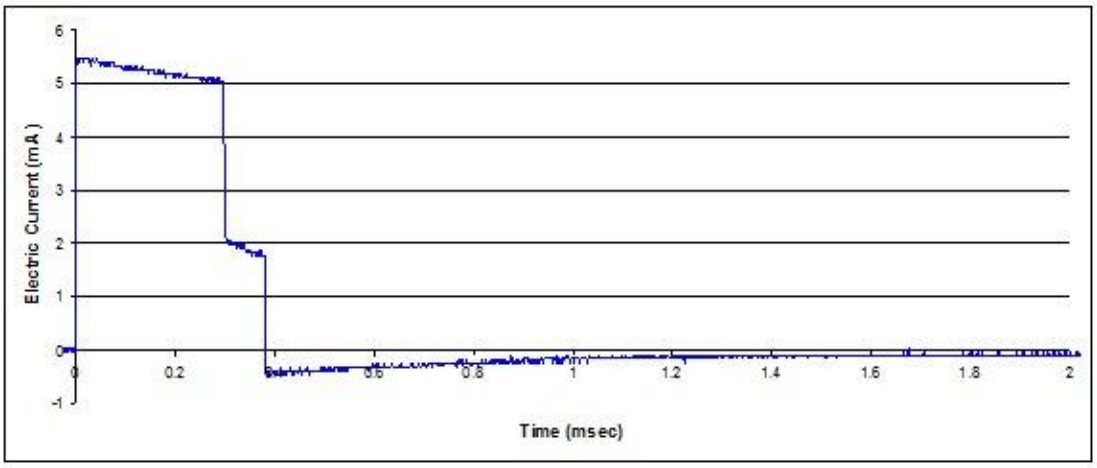

Figure 6: Recorded implantable neurostimulator output waveform.

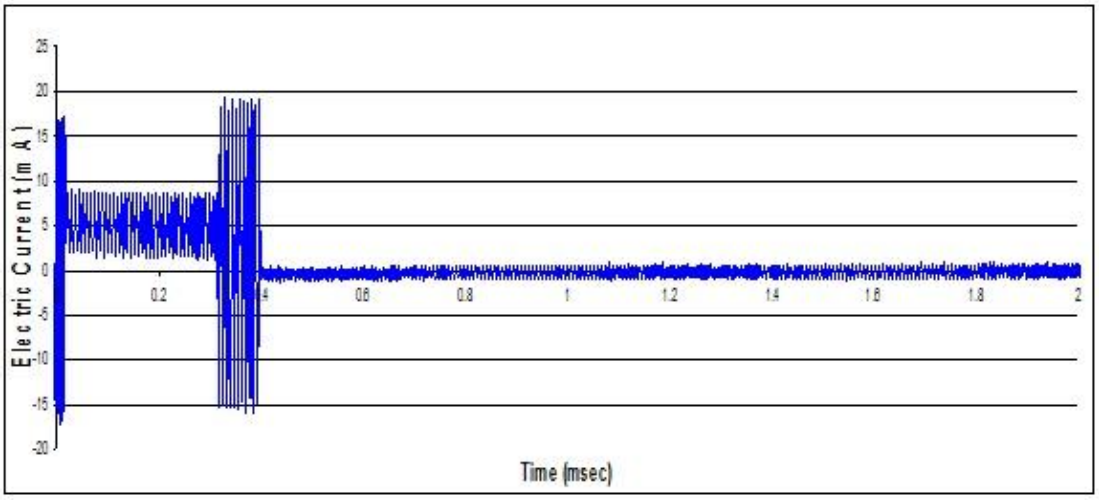

Figure 7: Recorded implantable neurostimulator output waveform when in close proximity to RFID emitter.

Next, we generated a time-ordered digital array of (x,y) pairs for each recorded output waveform. In the SENN model, we used the sampled temporal waveform option, IWAVE 13, which is commonly used to compute thresholds of temporal waveforms recorded from electrical devices. In our case, we used this model to compute threshold factors for excitation of spinal cord fiber. In order to process an array of

sampled date, the SENN model traces the waveform by indexing through the array and reading (x,y) pairs [21].

We recorded the output waveform from implantable neurostimulator three times; the SENN model generated three threshold multipliers of identical values, which were 0.22198. The reciprocal of 0.22198 is 4.5; this means that the waveform is 4.5 times larger in amplitude than needed to generate an action potential in spinal cord fiber. The reciprocal of a SENN threshold multiplier is also knows as a "threshold factor" or the ratio of applied stimulus to stimulus at threshold of excitation.

Additionally, we recorded three output waveforms from implantable neurostimulator with induced voltage caused by the RFID emitter. The SENN model generated three threshold multipliers, 0.2304, 0.2304 and 0.2264. The corresponding threshold factors are 4.34, 4.34 and 4.42 respectively. This means that the recorded waveform is 4.34 and 4.42 times larger in amplitude than needed to generate an action potential. We expected all reciprocals of threshold multipliers to be greater than unity in amplitude because the recorded waveforms were of parameters to stimulate a number of nerve fibers at a time.

Furthermore, one of the objectives of this study was to determine the severity of EMI caused by an RFID emitter. From the obtained multiplier thresholds, the results show that a stimulation pulse with EMI from an RFID emitter has an effect that is

equivalent to a smaller in amplitude stimulating waveform. We did further investigation and determined that the threshold factor of 4.34 in SENN model is equivalent to 5.1mA and 300 µsec output waveform from a spinal cord neurostimulator. Referring back to the study where we obtained best therapy parameters for stimulation [22], the study additionally lists a perception threshold of 4.6 mA in amplitude and 300 µsec in pulse width and a discomfort threshold of 6.0 mA in amplitude and 300 µsec in pulse width. Overall, the output waveform with amplitude of 5.1 mA is higher than the perception threshold and lower than discomfort threshold.

2.2.5. Discussion

Overall, we recorded waveforms with and without induced voltage from RFID emitter. The waveforms with induced voltage from RFID emitter received smaller threshold factors than recorded waveforms without the induced voltage. This could be due to the dominant set of waveforms generated by the neurostimulator system itself. We referred to published in literature on strength-duration relationships derived from the myelinated nerve models. The electric current thresholds for single-cycle biphasic stimuli with an initial cathodic phase and a point electrode that is 2 mm distant from 20 µm fiber are as follows. The current threshold for 300 µsec pulse width biphasic pulse is approximately 0.6 mA, while the current threshold of 7.46 µsec (low frequency RFID pulse of 134kHz) sine-wave pulse is approximately 40 mA [25]. The RFID pulse of 134 kHz in frequency is signification higher in frequency than pulses

generated by spinal cord neurostimulator system and therefore must be much higher in amplitude in order to generate an action potential.

In our case, the signal generated by the neurostimulator was set at 5.3 mA peak, which is larger than the reported 0.6mA peak. The RFID interference was recorded at approximately 18mA, which is below the needed amplitude of 40 mA to generate an action potential. When combined, in this case, the RFID interference caused a subtractive effect; the dominant waveform is minimized and therefore causes a slight reduction in threshold factors. This could be due to the way the neurostimulator system is designed to generate waveforms. In Figures 7, the period between 400 µsec and 2 msec, the interference recorded is at the minimum. This could indicate that the electrodes are connected to a high resistance inside the pulse generator. During switching times, between 0-20 µsec and 300-400 µsec of Figure 7, the interference is recorded at its maximum; this indicates that the electrodes are connected to a low impedance load inside the pulse generator. Between the times of 20 µsec and 300 µsec or when the pulse generator is outputting the monophasic pulse, it is not very clear how electrodes are connected internally without knowing the circuitry used for generating waveforms.

If the neurostimulator system was designed differently, for example having a low impedance connection between electrodes during the pulse output off period, this would cause a significantly greater voltage across electrodes in saline, therefore

causing a significant addition to the output waveform that could potentially have an additive effect on the stimulation threshold factor, possibly bringing stimulation parameters to discomfort level.

2.2.6. Limitations

The study was conducted on a phantom filled with saline solution representing the average conductivity of a spinal cord. The spinal cord is a complex structure consisting of various layers of nerve fibers, gray matter, white matter, cerebrospinal fluid and epidural fat; the electrical conductivities of which could vary in three orders of magnitude. Changes in electrical conductivities could results in changes of electrical current supplied by the neurostimulator system. The neurostimulator lead was configured for the worst case scenario for the specific RFID antenna used in this study. The worst case scenario represents the maximum coupling of electromagnetic fields into the neurostimulator system leads and therefore the largest induced voltages. Such a configuration does not represent the way such device would most likely be implanted. In addition, the SENN model was used to analyze output waveforms of a single spinal cord fiber. We applied this model to the best therapy stimulation parameters for one specific nerve fiber and not to all fibers in the spinal cord.

2.2.7. Conclusion

From the results of our analysis, we concluded that electric currents induced by coupling of magnetic fields from a LF RFID emitter to the leads of a neurostimulator do not bring the best therapy stimulation parameters below perception threshold stimulation parameters or above discomfort threshold stimulation parameters in one implantable neurostimulator system indicated for pain relief. Overall, we demonstrated a method for analyzing effects of coupled magnetic field interference on implantable neurostimulator systems and its electrodes which could be used by device manufacturers during the design and testing phases of the development process. This method could also be applied to other implantable devices such as pacemakers, implantable cardioverter defibrillators and other types of active implantable devices. Manufacturers of active implantable devices need to be aware of the potential risk of EMI from RFID emitters and design their medical devices appropriately. Additionally, RFID industry should take into account the potential effects on active implantable medical devices when designing, configuring and installing their systems. Moreover, patients and physicians should all be aware of the possibility of adverse effects of implantable neurostimulators from RFID emitters. In the future, our goal is to increase the number and variety of tested implantable neurostimulators.

3. Renewable Power for Implantable Neurostimulators

3.1. Background

All active implantable devices require power sources. The majority of implantable neurostimulators are powered by internal sources such as batteries. Batteries could also have a primary use (single use batteries) or a secondary use (rechargeable batteries). The power need of a particular neurostimulator depends on the neurostimulator's application, which highly depends on the number of channels used and stimulating characteristics [1]. Typical neurostimulator pulse parameters are; amplitude of 30mA, pulse width of 2 msec, and pulse repetition rate of 1500Hz [17]. The requirement for neurostimulators is to last for at least 5 years, however, previous studies have shown that in many cases the battery only lasts for up to 3 years [1].

For decades, implantable medical devices have been powered by reliable and predictable batteries based on lithium [1]. In pacemakers, same types of batteries are used and at the power output of 1μW, the lifetime of a battery in many cases exceeds 10 years [26]. Neurostimulors are also powered by lithium based batteries; however their power needs exceed those of a pacemaker. Non-rechargeable systems supply 3.5Volts and they draw anywhere from 80μA to several milli-Amps of current [1]. Due to growing power needs, rechargeable systems were introduced. Rechargeable system also operate on 3.3-3.7 Volts and draw anywhere between 50- 200 milli-Amps of current. The most common way of transferring power is through radio-frequency

coupling. In this case, an external coil is introduced to one that is implanted in the body [1]. Nevertheless, all current methods of powering implantable neurostimulators include batteries that contain potentially hazardous materials and depending on the power usage have to be surgically replaced within a few years insertion.

In recent years, the search for alternative power solutions has been increasing. A few examples include, nuclear power batteries that provide decade long lifetimes, but little patient acceptance. These types of batteries have short commercial success due to their cost, however, it has been claimed that less frequent reoperations outweigh the cost of the battery itself [1, 27].

A series of attempts have been made in harvesting energy from the human body itself. One example includes a device that has the ability to utilize the difference in temperature at different locations within patient's body [1, 28]. Another example includes a totally implantable system that is capable of harvesting power from electrically activated muscle [1, 29]. One of the recently developed examples is a substitution of a usual implantable device battery for a rechargeable battery, which is powered by a photovoltaic converter [30]. Yet, another example is a wrist-watch automatic generating system that is actuated by walking and body movement. Such a device has been placed directly on a beating heart and was capable of generating 13μJ of energy [31]. Some of the above stated examples share the same disadvantages as the current implanted batteries, such as, heating of the tissue, low cosmetic

acceptance, accurate positioning of the external device, and risk of infection [32]. On the other side, many of these examples are already developed systems that have numerous advantages over the presently used set of batteries; however many of them still need to be proven to be practical enough for commercial implementation.

We developed a system that is based on cascaded concentration cells that currently delivers a few μW of power and, if scaled, capable of powering small scale implantable devices. Ideally, the system could replace or charge an existing battery based on concentration differences that already exist within human body. Such concentration differences include; difference in oxygen in the blood running through the veins and arteries, the difference in glucose levels in various organs, as well as the difference in acid levels throughout the human digestive system. Our system effectively demonstrates the cascading of concentration cells to reach the desired levels of electrical potential. Such a cascading method is already utilized in nature, more specifically, in electric fish. This cascading method has been proven to work in theory [33]. Characteristics of our single concentration cell have been already established and published [35]. Our system has several advantages over the current implantable batteries and other proposed technologies. The most important advantage is the use of flexible biocompatible materials. Our system does not use toxic or nuclear materials. It does not depend on energy sources outside of the human body or body movement. It does not heat the tissue or require a cosmetic disadvantage. It makes use of renewable energy sources within the body.

3.2. Theory

3.2.1. Reverse electrodialysis

In theory, electricity can be produced by the mixing of two solutions of different concentrations. This phenomenon is called reverse electrodialysis. Typically, such a system is usually made of a compartment that holds a solution of high concentration, an ion exchange membrane, and another compartment that holds a low concentration solution. For example, consider cupric sulfate ($CuSO_4$) solutions of different concentrations. In this case, negative ions (SO_4^{--}) from a high concentration solution cell diffuses through the anion membrane to the low concentration solution cell causing negative potential and therefore electricity (or flow of electrons). The potential difference between solutions can be calculated using the Nernst equation.

$$E = \frac{RT}{zF} \ln\left(\frac{C_{high}}{C_{low}} \right)$$

where,

R: 8.314472 J K^{-1} mol^{-1} Universal Gas Constant

T: absolute temperature (Kelvin)

z: the valence of the ion

F: 9.6485309×10^4 C mol^{-1}, Faraday's constant

C_{high}: high solution concentration (M)

C_{low}: low solution concentration (M) [35].

This electrical potential could also generate electrical current, and power an electrical load it is connected to. The electrical current would depend on the resistance value of the load.

3.2.2. Internal Resistance

Internal resistance of a single cell reverse electrodialysis system is defined as a sum of resistances of a compartment that holds a solution of high concentration, an ion exchange membrane, and another compartment that holds a low concentration solution. Under the assumption of direct current, the capacitance component of a cell is neglected.

$$R_{internal} = R_{high\_concentraton\_compartment} + R_{membrane} + R_{low\_concentraton\_compartment} \quad [36]$$

and

$$R_{compartment} = \rho \frac{l}{A};$$

where,

ρ : resistivity (Ohm m)

l: length of the cell (m)

A: cross sectional area of the cell (m^2)

3.2.3. Efficiency & Power

The efficiency is defined as a ratio of power delivered to an external load to the total power dissipated. It has no units. This could be summarized in the following ratio,

$$\eta = \frac{I^2 R_{load}}{I^2 R_{internal} + I^2 R_{load}} = \frac{R_{load}}{R_{internal} + R_{load}}$$

The maximum power occurs when $R_{internal} = R_{load}$. In the case of $R_{internal} = R_{load}$, the efficiency cannot be higher than 50% [36].

3.2.4. Efficiency & Energy

Another way of defining efficiency is using the ratio of energy delivered to the load over the amount of energy stored in the concentration gradient. In order to determine the amount of energy stored in the concentration gradient, chemical potential between two solutions of different concentrations can be calculated. The amount of energy extracted from missing two solutions of different concentrations can be calculated using the Gibbs free energy of mixing. The relation is given by the following[36];

$$Gibbs\_free\_energy = 2RT(V_h C_h \ln\frac{C_h}{C_T} + V_L C_L \ln\frac{C_L}{C_T})$$

$$C_T = \frac{V_h C_h + V_L C_L}{V_T + V_L};$$

where,

R: 8.314472 J K^{-1} mol^{-1} Universal Gas Constant

T: absolute temperature (Kelvin)

Therefore, the efficiency in this case is defined as follows,

$$\eta = \frac{Energy_{Load}}{Gibb's\_Free\_Energy}$$

3.2.5. Power Density

The power density is defined as external power over the membrane area. It is measured in Watts/m^2. The maximum power density is when $R_{internal} = R_{load}$. A

literature search showed power densities achieved from sea and river water by different scientific groups varying from 0.05 – 0.95 W/m^2. The power density relation could be summarized in the following way,

$$Power\_Density = \frac{Power_{external}}{Area};$$

$$Power\_Density = \frac{I^2 R_{load}}{Area};$$

$$Power\_Density = \left(\frac{V_{cell}}{R_{internal} + R_{load}} \right)^2 \frac{R_{load}}{Area}; \qquad [36]$$

For maximum power density $R_{internal} = R_{load}$ then,

$$Power\_Density = \left(\frac{V_{cell}}{2R_{internal}} \right)^2 \frac{R_{internal}}{Area};$$

$$Power\_Density = \frac{V^2_{cell}}{4R_{internal} Area};$$

3.3. Methods

3.3.1. Single Cell Characterization

Prior to investigating the cascaded effect of multiple cells, it is important to study characteristics of a single cell. A mold was designed to make a cast containing 12 single cells, each one 7 mm thick and 5 mm in diameter. The casts were made from polydimethylsiloxane (PDMS) materials. They were also exposed to air plasma which allowed them to become hydrophilic and therefore reduce chances of forming air

bubbles during experiments. The power densities and temporal behavior of diffusion potentials across two different membranes were studied by my colleagues, Ramin Sadeghian and Daniel Tate. In their research, they studied the effects of Millipore and Fumasep FAD membranes. The Millipore membrane is a filtration type of membrane which allows anions and cations to pass through and filters based on the size of the ions. Fumasep FAD membrane is an ion exchange membrane which is selective to one particular type of ions. The layout of their concentration cell consisted of two layers of copper contacts on opposite ends made of copper tape, two layers of PDMS casts and a micro-porous membrane in the middle. Figure 8 demonstrates the layout of the single cell. The highest concentration solution was fixed at 1M of $CuSO_4$. The concentration solution ratio was varied in the following order, 2, 10, 20, 100, 200, and 1000. The power density was calculated by $P_{load}=V_{load}/(R_{load}\ A)$, where A is the area of the membrane.

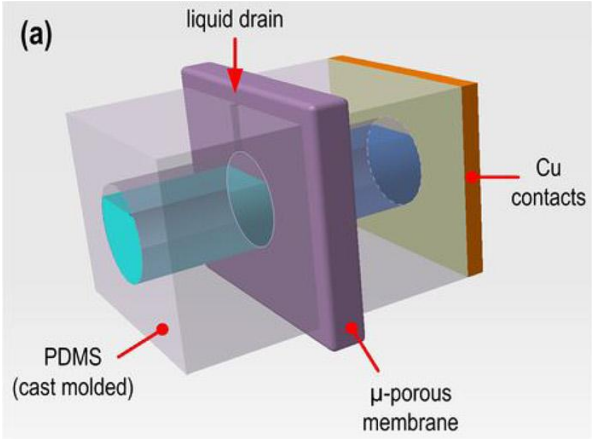

Figure 8: Layout of the single cell. Credits to Ramin Sadeghian and Daniel Tate.

The results of single cell characterization are shown in Figure 9. In conclusion of this study, it was shown that the Fumasep FAD membrane generates the highest power density of 0.7 μW/cm^2. Next, the optimum concentration ratio was found to be 50 with internal resistances of 5-10kOhms closely matched to load resistances for maximum power generation.

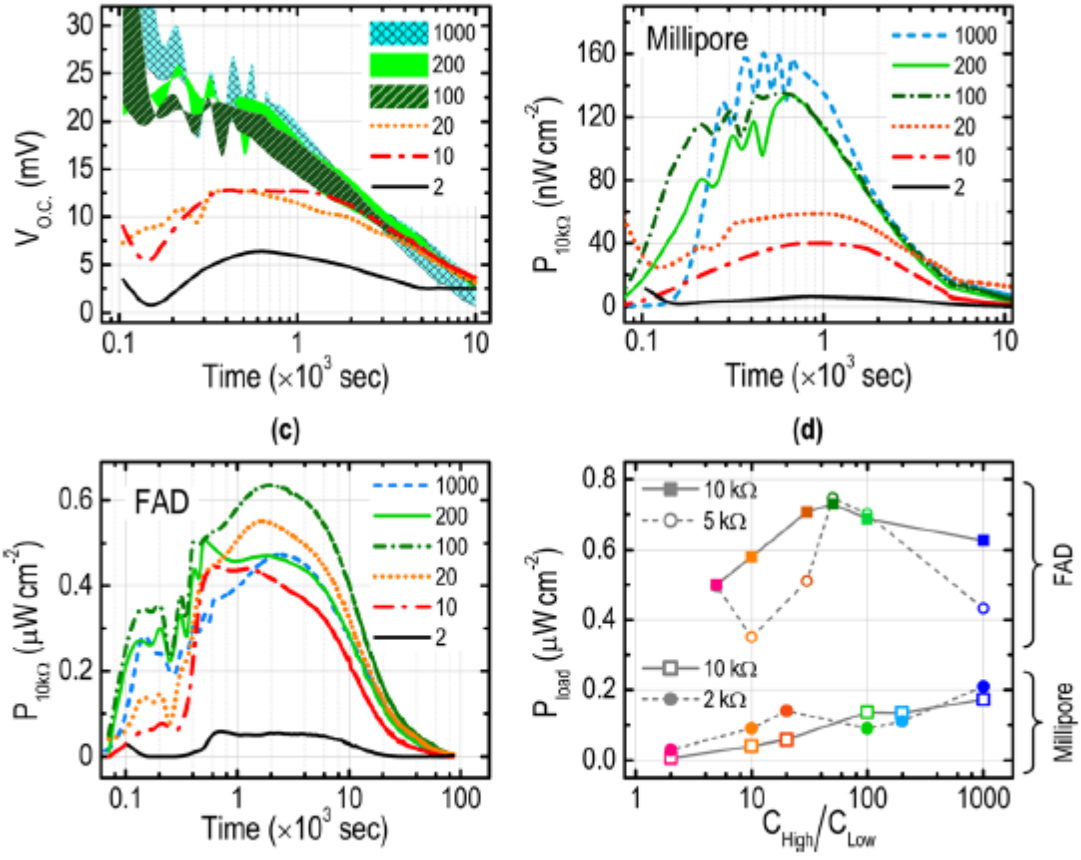

Figure 9: Results of single cell characterization by Ramin Sadeghian and Daniel Tate.

3.3.2. Cascaded cells

A design was submitted to e-machineshop.com for a fabrication of a master mold made from a Fluoropolymer Teflon material. This material was chosen based on its ability for easy release and separation from elastomeric materials. The overall mold was measured to be 80 x 30 x 5 mm. It contained 26 cylindrical structures to form cells and 4 rectangular microchannels for interconnection of those cells. Each cylindrical structure was 3 mm in diameter and 2 mm tall. Each microchannel was 7.1 mm long and 300 um x 200 um across. See Figure 10 for further details.

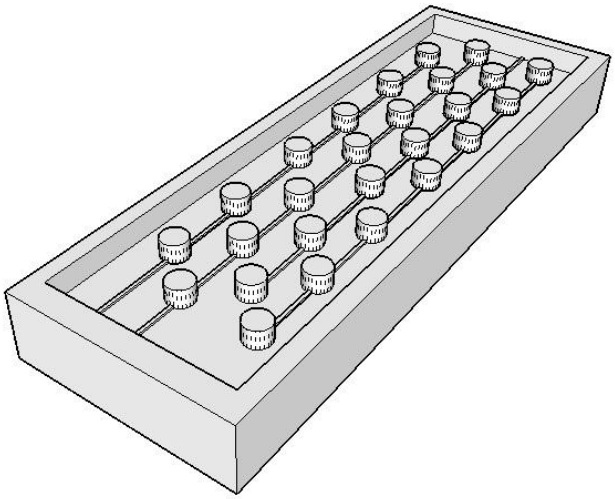

Figure 10: The layout of the master mold.

Dow Corning Sylgard 184 prepolymer and a curing agent were mixed with a ratio of 15:1, and then poured into the master mold. The mold was then left for 30 minutes for air bubbles that formed during mixing to come up to the surface and escape. The master mold was then cured for 20 minutes at 100°C in the oven and cooled off for 10

minutes afterwards. Using a razor blade and tweezers, the cast was removed from the master mold. The same procedure was repeated to make a second cast. The resulted casts were measured to be 76 x 25 x 2 mm which are the approximate dimensions of widely used microscope slides. Next, approximately 1 mm was cut around all the edges to remove any formed meniscus. An extra thin anion exchange membrane FAD from Fumasep (Germany) was used in between the cells of high and low concentration [37,38]. The membrane was cut into 26 of 0.3175 cm (⅛ inch) in diameter circles using a paper hole puncher (8645T9, McMaster-Carr). The 24 Gauge copper wire was cut into 1 cm long pieces and used to interconnect the cells of high and low concentration. Clear polycarbonate blocks with dimensions of 77 x 51 x 6 mm with 14 threaded 4-40 nc holes and 14 metal thumbscrews were used to secure the system.

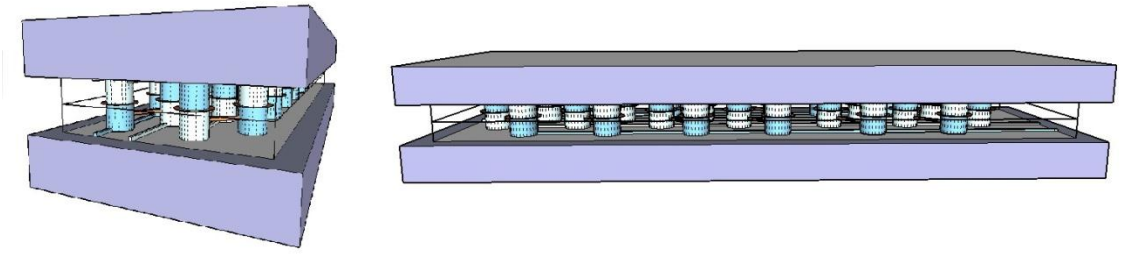

Figure 11: Front and side view of the overall system.

With all the parts ready, the system was then assembled in the following order. The first cast was placed on top of the first polycarbonate block with the channels facing towards the block. The cut out membranes were placed on top of every cell. The second cast with the channels facing away was placed on top of the membranes. The

second polycarbonate block was placed on top of the second cast. Lastly, the system was secured in place with 14 thumbscrews via through and threaded holes in polycarbonate blocks. See Figure 11 for further details.

With the cast system assembled, the two concentration solutions were made using Cupric Sulfate Anhydrous (Fisher Scientific, S75112) and filtered deionized water (filter system by Barnstead E-Pure). The one molar (1M) solution was made by mixing 3.19 g of $CuSO_4$ with 20 mL of deionized water. Other concentrations of 0.1M, 0.01M, 0.001M were made by diluting 1M $CuSO_4$ solution respectively. Different concentration solutions were then transferred to 10mL syringes with needles.

Using copper wire of the same gauge, the low concentration compartment of the first cell and the high concentration compartment of the last cell were then connected to the recording instrument. The measurements were carried out using a Gamry Reference 600 Instrument with the Open Circuit Potential Setting. The system was set to high input impedance of 10GOhm with a sampling rate of 1Hz recording for a total of 5,000 seconds. The electrical potential in Volts was plotted against time in seconds.

Next, the recording was initiated before the filling process. The compartments intended for low concentration were filling in with the lower concentration solution

first followed by filling the compartments of the high concentration solution. As mentioned previously, the compartments of high and low concentration solutions were interconnected in a series with copper wire. See Figures 12 and 13 for detailed images of the filled in system and photographs of the filling in process.

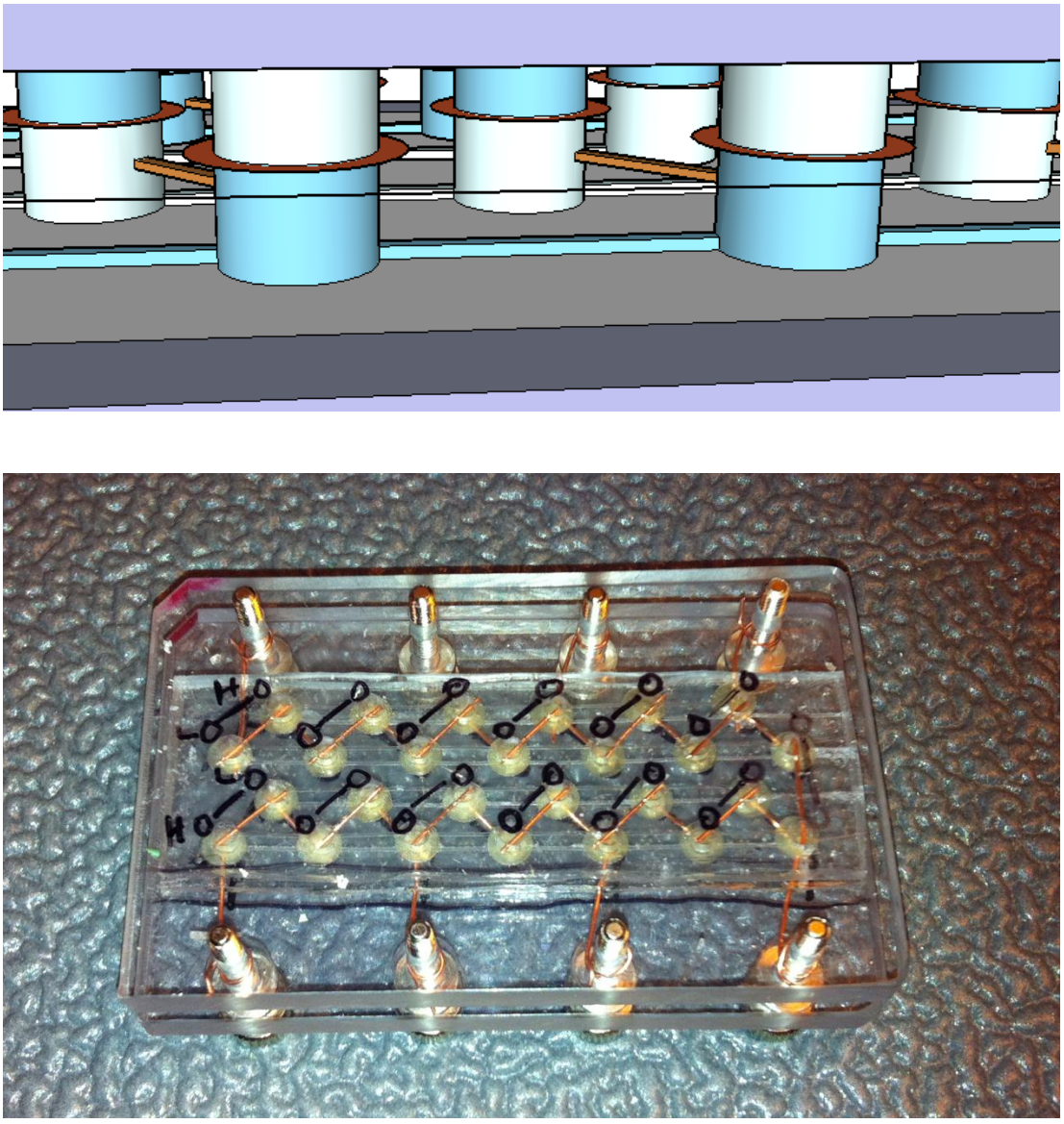

Figure 12: A. A cartoon image showing a stack of casts with solutions filled in cells and channels. B. A photograph showing actual device from an angle view. In this case, earlier version of the device is showing which includes eight thumbscrews.

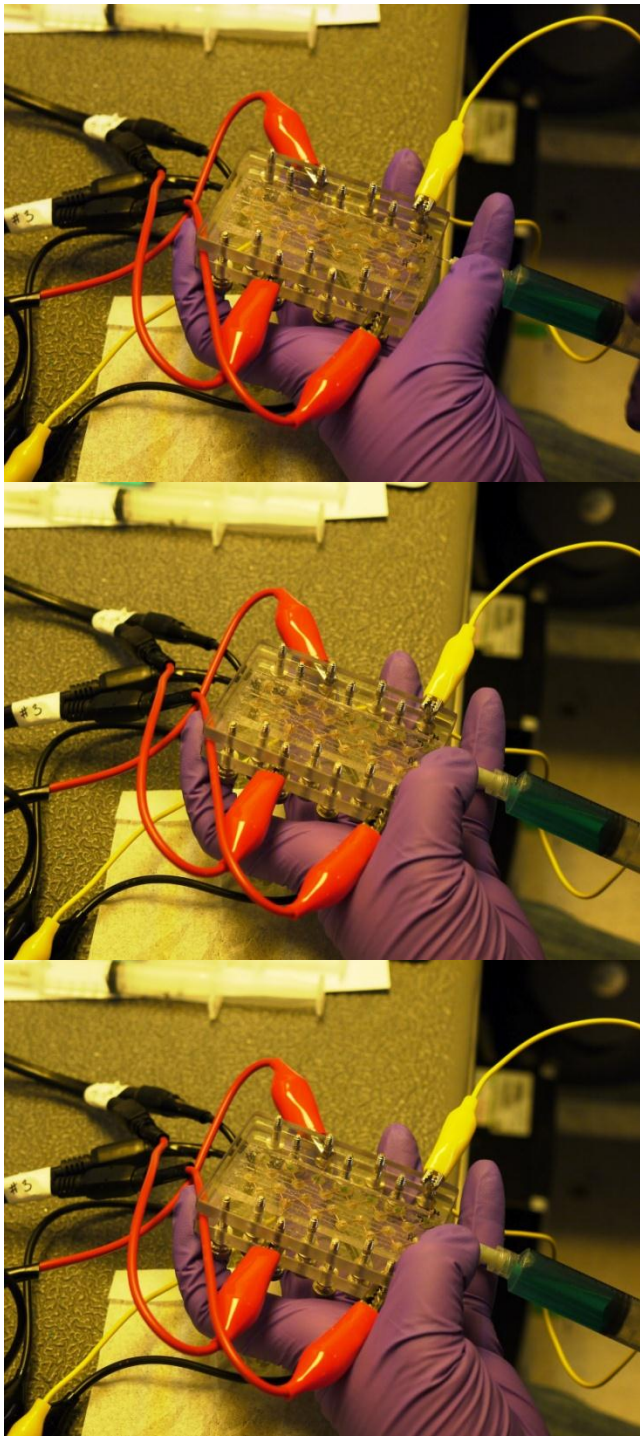

Figure 13: A series of photographs demonstrating filling in process of high concentration solution. The alligator clips are connected to the 1st, 9th, 17th and 26th cell.

3.4. Results

A total of five experiments, each repeated three times, were conducted. An average of three repeated runs, the positive and negative errors were calculated and plotted at every 250 seconds interval. In the first three experiments, a load connected to the last (compartment of high concentration of the 26th) cell was varied. The three different loads were 500kOhm, 1MOhm and open circuit (10GOhm internal impedance of recording instrument). Figure 14 demonstrates a summary of recorded potentials. Appendix A contains plots of individual curves with error bars included. Figure 15 demonstrates the experimentally recorded electrical potentials recorded at the 1^{st}, 9^{th}, 17^{th}, and 26^{th} cells throughout one recording system, as well as, theoretically calculated peak voltages. Figure 16 demonstrates the electrical potentials recorded at the last cell with concentration ratios of 10, 100 and 1000.

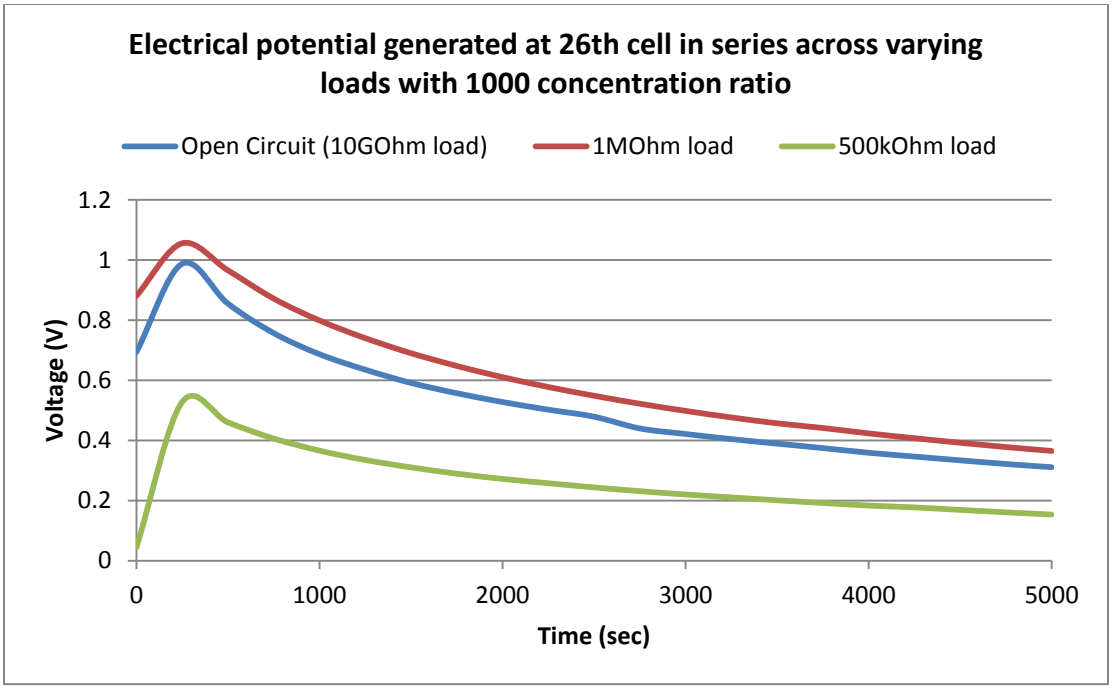

Figure 14: Electrical potential generated at 26th cell in series across varying loads with 1000 concentration ratio. Electrical loads of 10GOhm (open circuit, 1MOhm and 500kOhm) are shown.

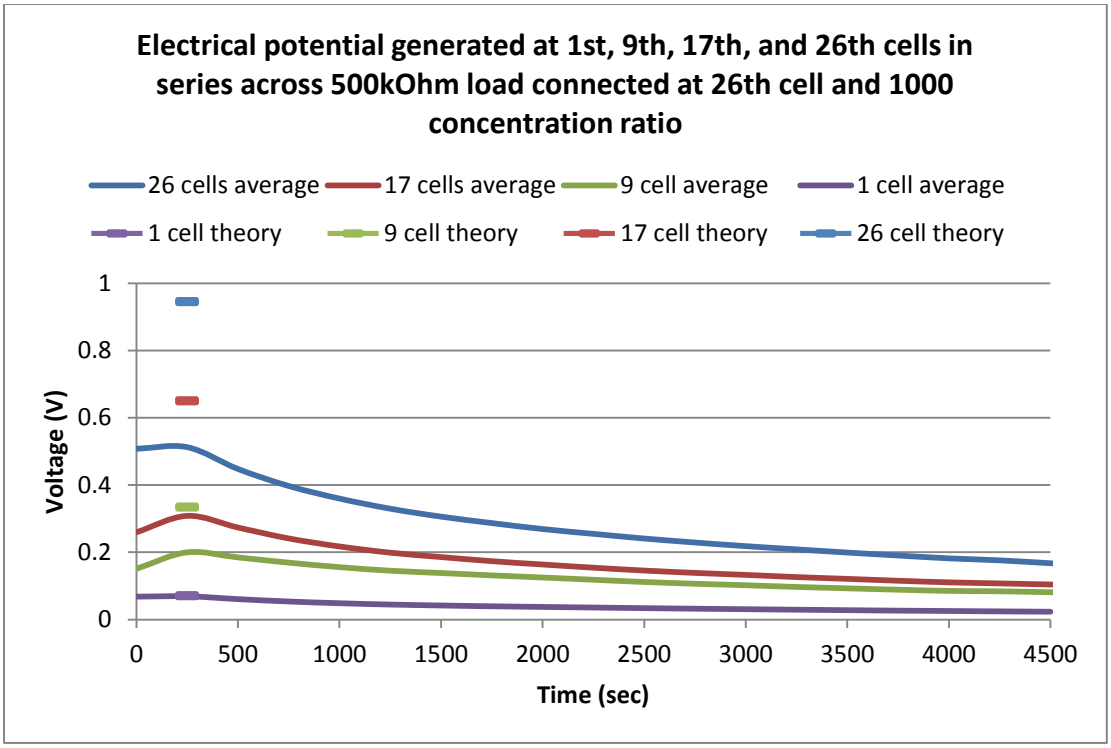

Figure 15: Electrical potential generated at 1st, 9th, 17th, and 26th cells in series across 500kOhm load connected at 26th cell and 1000 concentration ratio.

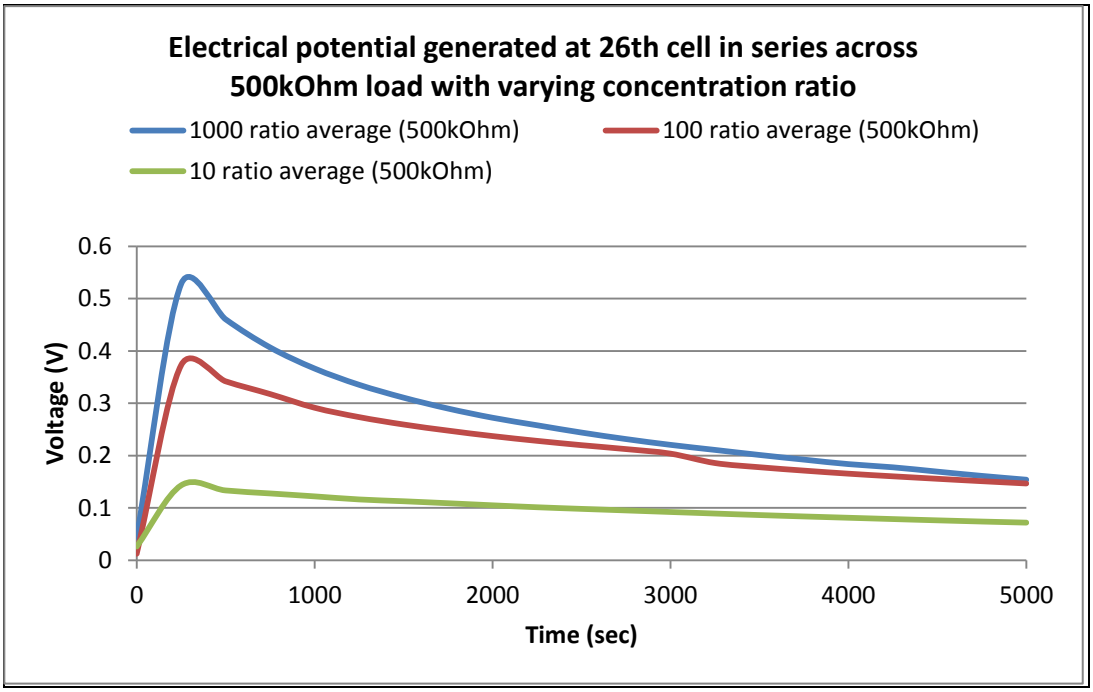

Figure 16: Electrical potential generated at 26th cell in series across 500kOhm load with varying concentration ratios. Concentration ratios of 1000, 100 and 10 are shown.

3.5. Analysis and Discussion

3.5.1. Calculating Electrical Potential Energy

Solutions of four different concentrations were considered (1M, 0.1M, 0.01M and 0.001M). Experiments were conducted with the following concentration ratios of $CuSO_4$, 1000, 100 and 10.

In the case of the high concentration solution of 1M and low concentration solution of 0.001M, the generated electrical potential is:

$$E = \frac{0.02585}{2} \ln\left(\frac{1MCuSO_4}{0.1MCuSO_4}\right)$$

$$E \approx 30mV$$

In the case of the high concentration solution of 1M and low concentration solution of 0.001M, the generated electrical potential is:

$$E = \frac{0.02585}{2} \ln\left(\frac{1MCuSO_4}{0.01MCuSO_4}\right)$$

$$E \approx 60mV$$

In the case of high concentration solution of 1M and low concentration solution of 0.001M, then the generated electrical potential is:

$$E = \frac{0.02585}{2} \ln\left(\frac{1MCuSO_4}{0.001MCuSO_4}\right)$$

$$E \approx 90mV$$

3.5.2. Calculating internal resistance

Calculating internal resistance of a multiple cell system where the cells are connected in series with fluidic channels of resistance that cannot be neglected, requires electric circuit analysis. In this case, 26 cells are in a series and interconnected with fluidic channels. Overall, the system contains eight channels (four channels of high concentration solution and four channels of low concentration solution per experiment). Each cell is 2 mm tall and 1.5 mm in diameter. Each channel is 7mm long and has a cross section of 200um x 300um. The resistance of those channels can

be calculated using the same equation as for $R_{compartment}$. Table 5 shows the calculated resistance values of compartment and cells of various concentrations.

Table 5: Calculated theoretical resistance values.

Molarity	Conductivity (mS/cm)	Resistivity (Ohms mm)	$R_{compartment}$ (Ohms)	$R_{channel}$ (Ohms)
1M	38.23	262	74	30.5k
0.1 M	7.541	1.3k	375	155k
0.01 M	1.392	7k	2k	838k
0.001 M	0.292	34k	9.7k	4M

The same type of membrane was used on all 26 cells. The resistance of this membrane can be calculated using the electrical resistance listed in the FumaSep FAD datasheet [38]. The listed value is 0.8 Ohm cm^2. The cross sectional area of the membrane is $\pi(0.15cm)^2$ and therefore the membrane resistance is,

$$\frac{0.8}{\pi(0.15cm^2)} = 11\ Ohms;$$

The internal resistance of the whole system can be determined by analyzing the equivalent circuit. Figure 17 demonstrates the equivalent electrical circuit of the overall system. A single cell is shown as a voltage source and internal resistance of a cell, denoted as, R_c. Internal resistance of a cell was calculated as follows,

$$R_{cell} = R_{high\_concentraton\_compartment} + R_{membrane} + R_{low\_concentraton\_compartment} \qquad [36]$$

Table 6 shows the calculated resistance values of a single cell, channel, and overall internal resistance of the whole system.

Table 6: Calculated resistance values of a single cell, channel and overall internal resistance of the whole system.

Concentration Ratio	R_{cell} (Ohms)	$R_{channel\ high\ conc.}$ (Ohms)	$R_{channel\ low\ conc.}$ (Ohms)	$R_{internal}$ (Ohms)
1000	9.7k	30.5k	4M	129k
100	2.1k	30.5k	838k	44.3k
10	460	30.5k	154k	11k

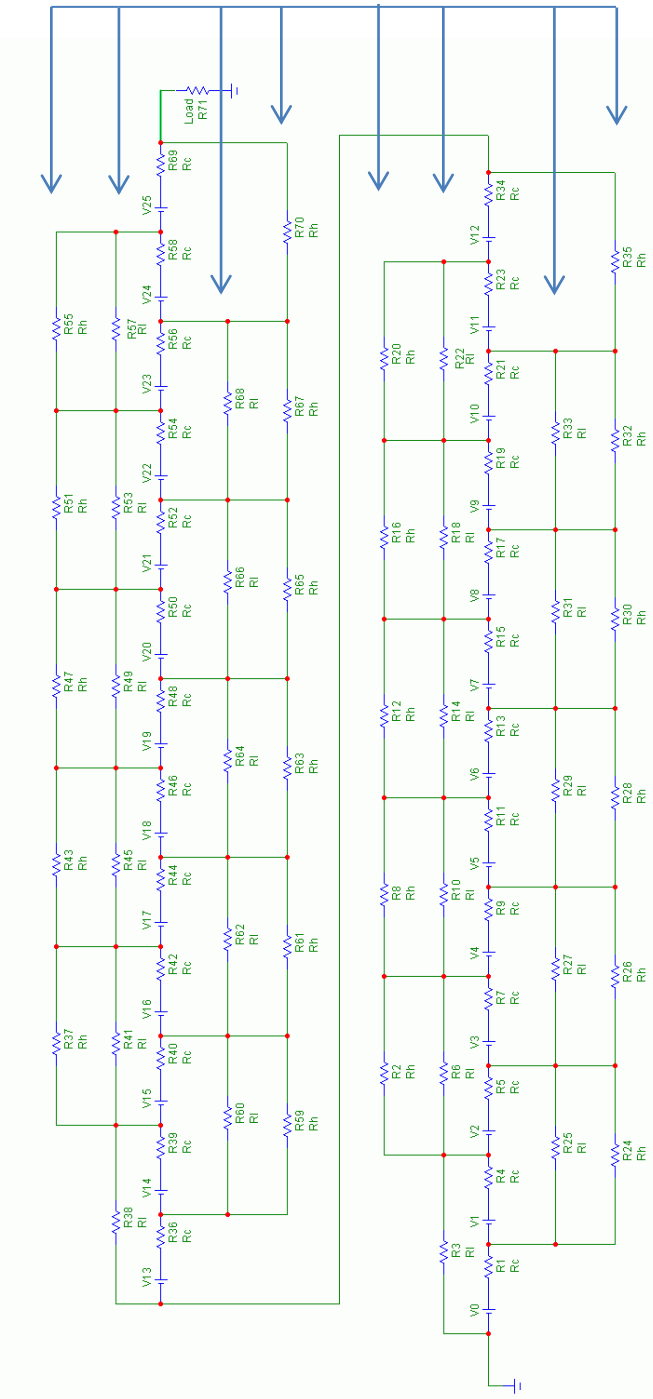

Figure 17: Equivalent circuit model of a system with 26 concentration cells connected in series. R_c is defined as resistance of a cell (sum of resistances of compartments with high and low concentrations and membrane resistance). R_h is the resistance of a channel filled with high concentration solution. R_l is the resistance of a channel filled with low concentration solution. V is the voltage generated by a single cell. Arrows at the top of the image indicate rows of fluidic channel (or shunt resistances).

3.5.3. Calculating theoretical peak voltage

The electrical potential across 10GOhm, 1MOhm, and 500kOhm loads is calculated using the circuit analysis of the equivalent circuit shown in Figure 17. The R71 resistor, also labeled as "Load", is the load resistance that was varied. The results for peak voltage are shown in Table 7.

Table 7: Calculated electrical potential across 10GOhm, 1MOhm and 500kOhm load.

Concentration Ratio	**Voltage $_{cell}$ (V)**	**R $_{cell}$ (Ohms)**	**R $_{channel\ high\ conc.}$ (Ohms)**	**R $_{channel\ low\ concentration}$ (Ohms)**	**R $_{load}$ (Ohms)**	**V $_{peak}$ (V)**
1000	0.09	9.7k	30.5k	4M	10G (open circuit)	1.19
					1M	1.05
					500k	0.95
100	0.06	2.1k	30.5k	838k	10G (open circuit)	1.26
					1M	1.21
					500k	1.16
10	0.03	460	30.5k	155k	10G (open circuit)	0.74
					1M	0.73
					500k	0.72

3.5.4. Comparing theoretical to experimental peak voltages

In this case, the theoretical voltage peaks stated in Table 7 are compared to the experimental values shown in Figures 14-16. The results of such comparison are shown in Table 8. The theoretical values of the 1000 concentration ratio, for a resistive load of 1MOhm and 10GOhm (open circuit) fall within the range of experimental values that were recorded. For the rest of the data, the theoretical values were much higher than the experimental values that were recorded. This could be due

to a lower channel resistance and, therefore, a lower overall internal resistance of the system.

Table 8: Theoretical and experimental values of electrical potentials.

Concentration Ratio	R_{load} (Ohms)	$V_{external\ theoretical}$ (V)	$V_{external\ experimental}$ (V)
1000	10G (open circuit)	1.19	0.75 - 1.15
	1M	1.05	0.77 - 1.43
	500k	0.95	0.51 - 0.57
100	500k	1.16	0.22 - 0.49
10	500k	0.72	0.11 - 0.2

3.5.5. Calculating efficiency & power

As mentioned previously, the efficiency is a ratio of power delivered to an external load to the total power dissipated. It is calculated from the values found in Table 2. The results of such calculations are shown in Table 9. The efficiency is the highest for the concentration ratio of 1000 system. In this case R_{Load} is much higher than $R_{internal}$ and, therefore, the denominator of the efficiency relation dominates resulting in higher efficiency.

Table 9: Efficiency is calculated using the following relation, $\eta=R_L/(R_L+R_{internal})$.

Concentration Ratio	$R_{internal}$ (Ohms)	R_{load} (Ohms)	η
1000	129k	1M	0.89
		500k	0.79
100	44.3k	500k	0.92
10	11k	500k	0.98

3.5.5. Calculating efficiency & energy

As mentioned in Chapter 3.2.4. of this dissertation, the overall efficiency can also be calculated using the ratio of energy across the load resistance over the chemical potential energy between two solutions of different concentrations. In this case,

$$Gibbs\_free\_energy = 2RT(V_h C_h \ln\frac{C_h}{C_T} + V_L C_L \ln\frac{C_L}{C_T})$$

$$C_T = \frac{V_h C_h + V_L C_L}{V_T + V_L};$$

where,

R: 8.314472 J K^{-1} mol^{-1} Universal Gas Constant

T: absolute temperature (Kelvin)

$$Gibbs\_free\_energy = 1228mJ;$$

To calculate experimental energy, an integral of the power vs. time curve was taken of the experiment with a concentration ratio of 1000 and 1MOhm load.

$$Energy_{experimental} = 4.4mJ;$$

$$Efficiency = \frac{4.4mJ}{1228mJ};$$

$$Efficiency = 0.36\%$$

3.5.6. Calculating power and power density

The power density of the system can be defined in two distinct relations. First, it could be defined as the maximum power over the area of the system. The unit of such power density is W/m^2. A literature search showed that in the last decade power densities achieved for single cell by different scientific groups for river and sea water varied from 0.05 – 0.95 W/m^2. A work published by Sadeghian *et. al.* showed the power density for a single cell varying from 0.2 – 0.7uW/cm^2 . In this case, one single cell (2mm tall, 1.5 mm in radius with concentration ratio of 1000 and R_{load} of 500kOhm) resulted in peak electrical potential of 85.7mV, and therefore power density of 0.21uW/cm^2. The second relation for the power density is the maximum power generated over the volume of the system. The unit of such power density is W/m^3. Table 10 shows the power density calculated from the experimental values in both cases. According to the calculated values, the system with the concentration ratio of 1000 and R_{load} of 1MOhm, generates the most power, 2 µW, and has the highest power density of 1.11$\mu W/cm^2$ and 2.78 μWcm^3. The power density could be increased by reducing the internal resistance. This could be accomplished by decreasing thickness of each cell, however, this would cause a shorter overall discharge time.

Table 10: Power Density. The area used 1.84 cm^2 and volume used 0.74 cm^3.

Concentration Ratio	R_{load} (Ohms)	$V_{max\ experimental}$ (V)	Power (W)	Power Density ($\mu W/cm^2$)	Power Density ($\mu W/cm^3$)
1000	1M	1.43	2.0449E-06	1.11	2.78
	500k	0.57	6.498E-07	0.35	0.88
100	500k	0.49	4.802E-07	0.26	0.65
10	500k	0.19	7.22E-08	0.039	0.10

3.5.7. Investigating power & energy vs. concentration ratio

Theoretical and experimental power can be easily calculated using the simple power relation, power = voltage^2 / resistance. For the calculation of theoretical power, the simulated peak voltages were used from Table 7. For the calculation of experimentally generated power, the peak recorded voltage levels were used from Table 8. The results from both calculations are shown in Table 11. Furthermore, Figure 18 demonstrated such results graphically. In this case, it is clearly shown in theory that the power levels peaks at the concentration levels of 100, indicating optimum power, the experimentally generated power in fact shows continuous increase.

Table 31: Comparing theoretically simulated to experimentally generated power across 500kOhm load.

Concentration ratio	Power $_{theoretical}$ (W)	Power $_{experimental}$ (W)
1000	1.81E-06	6.50E-07
100	2.69E-06	4.80E-07
10	1.04E-06	7.22E-08

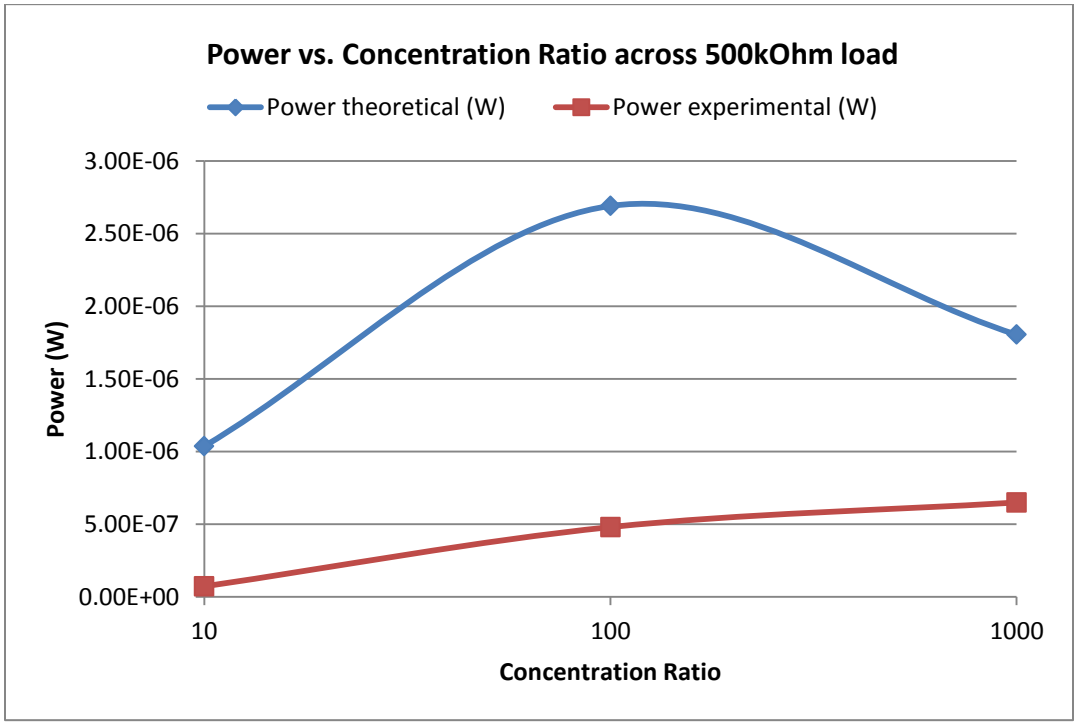

Figure 18 Comparing theoretically simulated and experimentally generated power across 500kOhm load.

Next, the theoretical and experimental generated energy were compared. The experimental energy was calculated by taking the integral of over power curve over time shown in Figure 16. In this case, the load resistance of 500 kOhm was used. The theoretical energy was calculated in the following way,

$$Energy = \frac{Power_{theoretical\ peak} * 5000\ seconds}{2}$$

Table 12 shows calculated results and Figure 19 shows graphical representation of such results. In this case, the levels of generated energy do not match again, however, they both show peak at the concentration ratio of 100 and therefore again indicating an optimum power level.

Table 14: Comparing theoretical and experimental energy generated across 500kOhm load.

Concentration ratio	Energy $_{theoretical}$ (J)	Energy $_{experimental}$ (J)
1000	0.0045125	0.000982
100	0.006728	0.001032
10	0.002592	0.000173

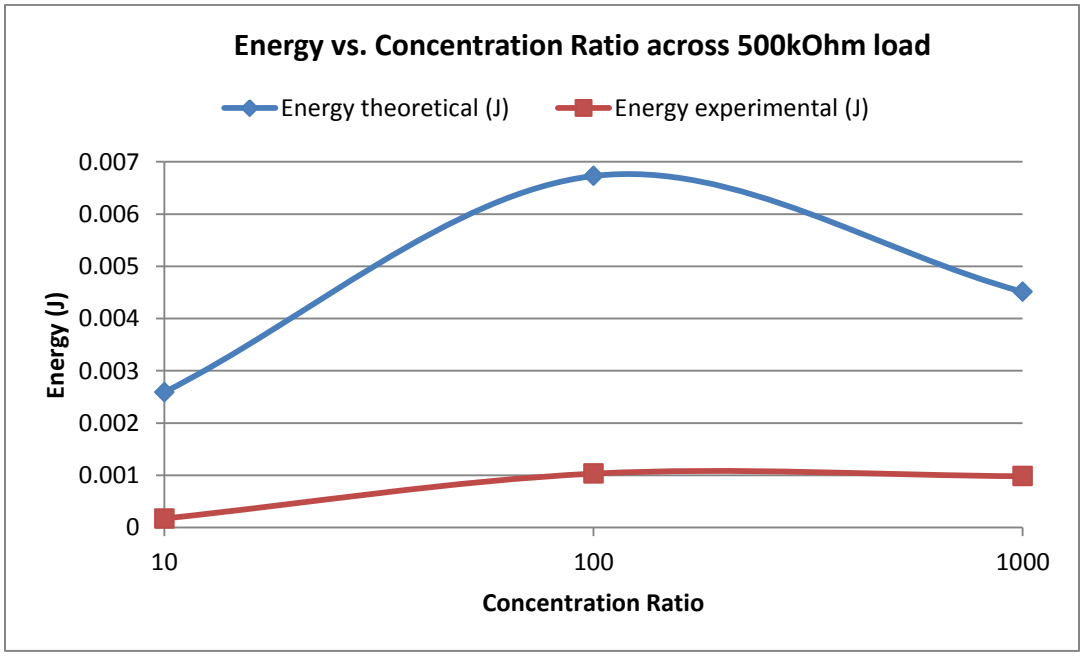

Figure 19 Comparing theoretical and experimental values generated across 500kOhm load.

3.5.8. Investigating power vs. load resistance

One important aspect of this study is to investigate theoretical power levels and experimental power levels versus their load resistances. In this case, the theoretical power level was calculated in the same way as shown in Chapter 3.2.2. of this dissertation using voltage peak values from Table 7. The experimental power was calculated using recorded maximum peak values shown in Table 8. Next, the results of such calculations are plotted in Figure 20. The data is plotted for the concentration ratio of 1000. In this case, in theory, the generated power is maximum occurs at 100kOhm load resistance, indicating that internal resistance is also 100kOhm. This agrees with the simulated values stated in Table 6. On the other hand, experimentally collected data disagrees with the theory. In this case, according to Figure 20, the optimum power occurs at the resistance of 1MOhm. This could be due to the usage and lifetime of flexible materials that casts are made of. With extended usage, the material was getting worn out causing fluidic channels to change and therefore increasing the overall impedance of the system.

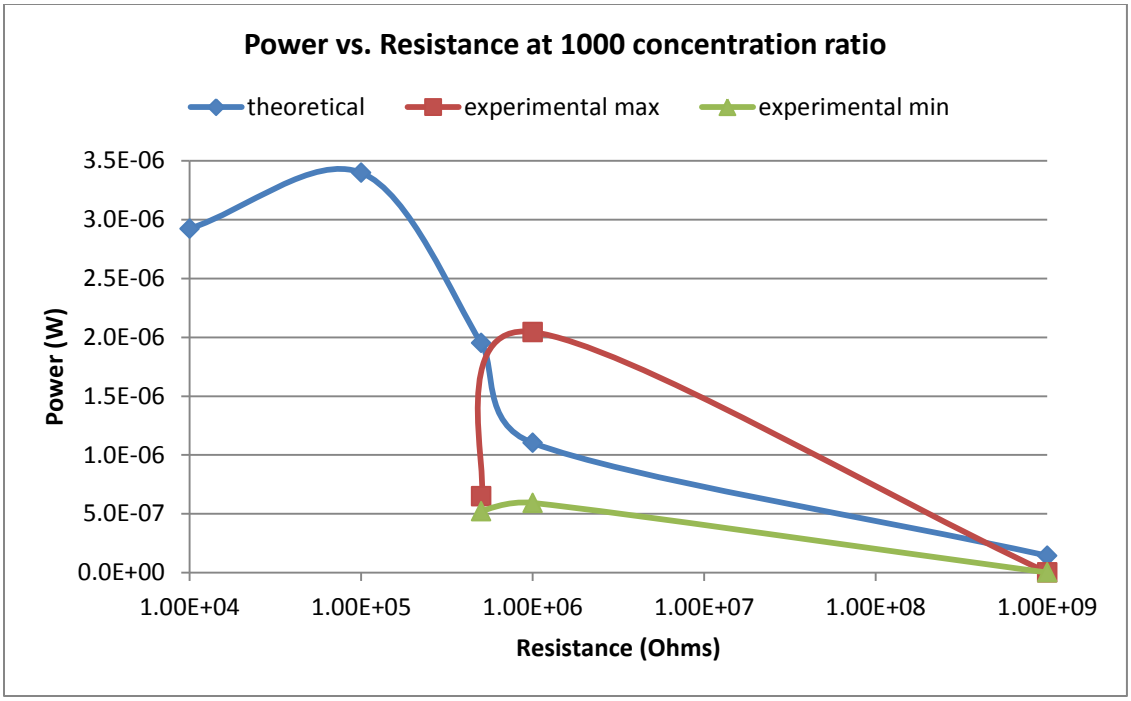

Figure 20 Comparing theoretical and experimental generated power while varying load resistance. In this case, example of concentration ratio of 1000 was investigated.

3.5.9. Calculating lifespan

The lifespan of the concentration cells heavily depends on its electrodes. In this case, the electrodes are made of copper metal. The calculation for electrochemical deposition is performed. The following relation is used in determining thickness of copper thickness transferred per single discharge.

$$Thickness = \frac{M_w}{nFAD} \int Idt \qquad [39]$$

where,

M_w: atomic weight

n: number of electrons taking point in reduction

F: 9.6485309×10^{4} C mol^{-1}, Faraday's constant

A: area of the deposit (cm^2)

D: density of metal

Substituting known parameters results in the following,

$$Thickness = \frac{63.546gr}{2*96{,}485C/mol*0.11cm^2*8.96gr/cm^3}\int Idt$$

$$Thickness = 0.00033\int Idt$$

Considering the experiment with highest calculated power, which is with 1000 concentration ratio and 1MOhm load. Experimentally, the peak voltage was recorded at 1.43V, therefore resulting current is 1.43 μA. See Figure 19 for further details.

$$Thickness = 0.00033*\frac{1}{2}*1.43\mu A*5000\sec$$

$$Thickness = 1.18*10^{-6}cm$$

$$Thickness = 12nm$$

Therefore, at the wire diameter of 0.511mm and the thickness deposition and release of 12 nm per cycle allows to have over 20,000 cycles. In order to extend the lifespan of electrodes even further, one could explore the possibility of alternating concentration solutions when filling up compartments. In this case, the positive and negative end electrical potentials would also need to be alternating.

3.6. Previous iterations

In the previous sections of this chapter, through carefully derived methods and analysis, a prototype of a system capable of powering small scale implantable devices was demonstrated. Many iterations and modifications were considered before making of a working prototype capable of reaching 1V of electrical potential. In order to recognize the effort made in developing the final working prototype, this section will be dedicated to a discussion of all previous iterations and prototypes.

The goal of the first prototype was to demonstrate the cascading effect (addition of electrical potentials) experimentally. A soft copy of the preliminary design was submitted to the Baskin Engineering Machine Shop. Within one month, a prototype was received back. It was made of polycarbonate see-through material. It contained 16 cells in a matrix of 4x4 cells. The cells were connected on the outside through a series of garden tubes. Figure 21 contains photographs of the first prototype. The maximum open circuit potential recorded was 100mV from 6 cells connected in series. Using this prototype, the proof of the cascading effect was achieved. In this prototype, the membrane was kept as one part with concentration cell compartments located around it. There were a few problems with this prototype, to state a few; it contained a lot of leaks and the channels were only as twice as thin as the cells themselves which contribute to a short (approximately 10min) discharge time. For the next iteration of prototypes, the goal was to miniaturize the system in size.

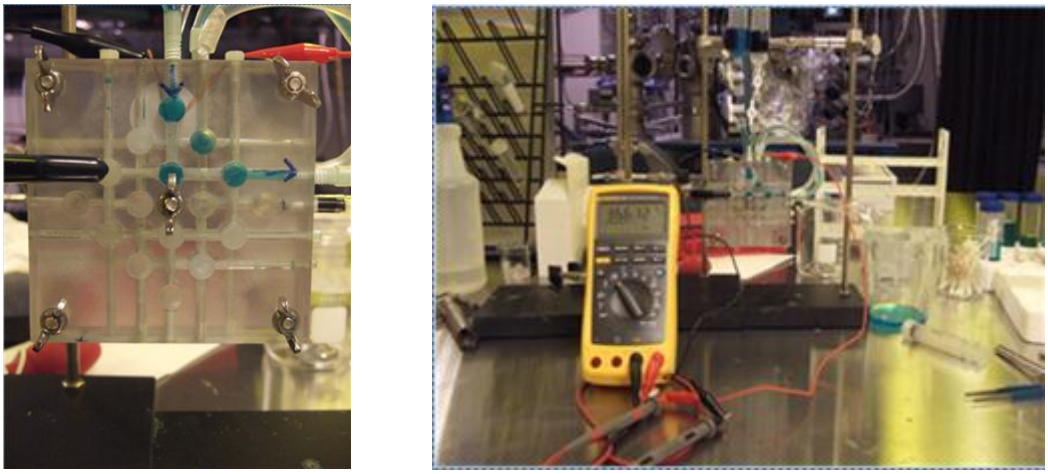

Figure 21 Two photographs showing the very first prototype in detail.

The second prototype was four times smaller than the first prototype. It contained eight cells in series connected through a copper wire. It is in this prototype when the elastomeric materials were used for the first time. In this case, the cells were now made by hand and were spherical, approximately 5mm in diameter. The system was secured together by paper clips. Also it is important to note that a metal mesh was used in the middle of each cast to make the device sturdier. Figure 22 demonstrates the layout of such device and recorded potentials. It is through this prototype that the cascaded effect was investigated with a greater number of cells in series and learned that by cascading fewer than 30 cells in series, an electric potential of 1V could be achieved. A few problems were encountered with this prototype. For example, the cupric sulfate solution was reacting with the metal mesh used inside casts. There were no observed leaks in this prototype. The next goals were to improve the prototype by eliminating the metal mesh grid and hand-making process of making cells.

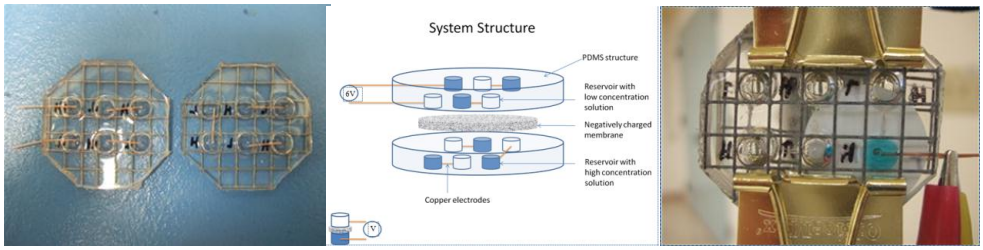

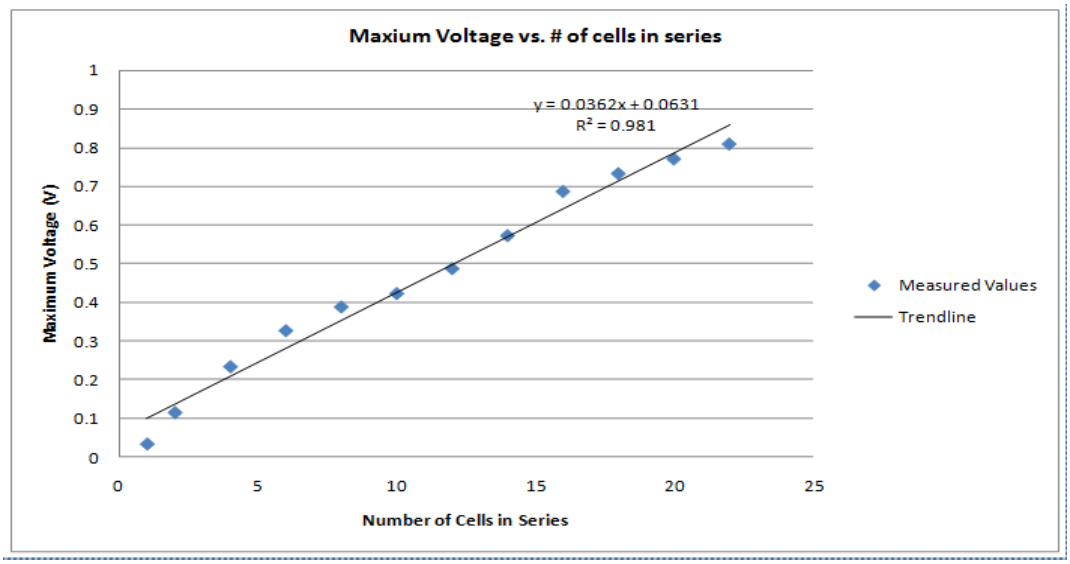

Figure 22 Top Left: a photograph of two casts used in assembling second prototype. Top middle: a schematic demonstrating insides of a prototype. Top right: assembled prototype with one cell filled in. Bottom middle: results of cascading 24 cells in series.

In the third prototype, the metal mesh was eliminated and replaced with two microscope slides in order to secure the system in place. In order to eliminate hand-made cells, a layout was submitted to emachineshop.com for a fabrication of a mold made of Teflon materials. The mold allowed the make of identical cells for every experiment. Again, the elastomeric materials were used to fill in molds and therefore make casts. In this design, additional channels were fabricated for air release during filling procedure. In this design, a total of 12 cells were made. See Figure 23 for

further details. It was this design that was used by Ramin Sadeghian and Daniel Tate to characterize single cells [34]. The details of this study will be discussed in the next section. The shortfalls of this design included the absence of fluidic channels connecting compartments of the same solution. In this design, a problem with cascading was discovered, the cells in series were no longer adding up as in previous prototypes. Through a thorough investigation, it was learned that a wet membrane allowed leaking between the channels and therefore prevented adding up of built up potential. The next goal was to further miniaturize the design and to achieve 1-2V electrical potential.

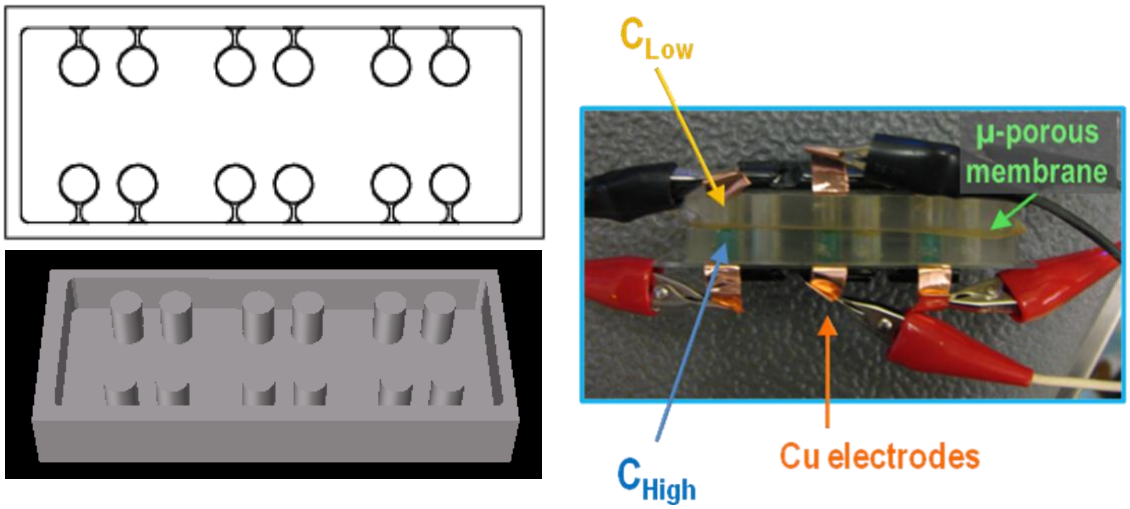

Figure 23 Third prototype shown in more detail. Topleft : layout submitted to emachineshop.com Bottom left: simulated 3D model. Right: single cell layout, 3 cell experiment [34]

The fourth design is the last iteration before the working prototype was achieved. Here, the cells were made thinner and therefore reduced the overall internal resistance of the system. There were 26 sells in series overall with eight fluidic channels interconnecting compartments of the same solutions. Figure 24 shows the layout in

further detail. The results that were achieved from this prototype were promising. From 21 cells connected in series without fluidic channels (sealed channels), a 1Volt of electrical potential was able to be reached. In this case, individual membranes were used for every cell. As with any other iteration, a number of problems were observed. The most important problem was that fluid was not passing through 100 x 100 µm designed fluidic channels and causing clogs along the way. From this design, it was yet proved again the concept of cascading cells.

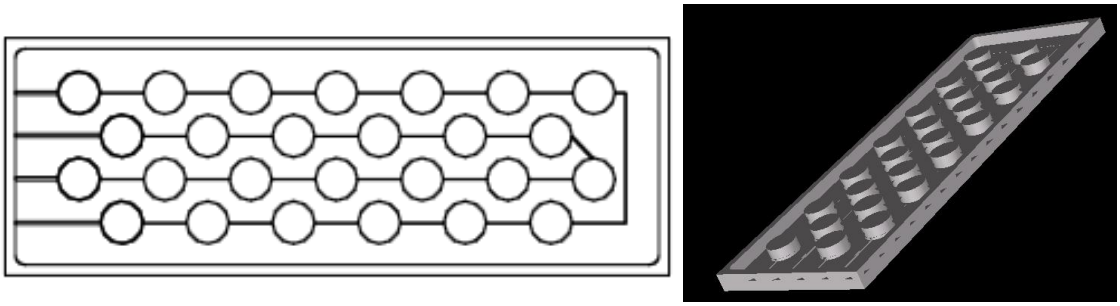

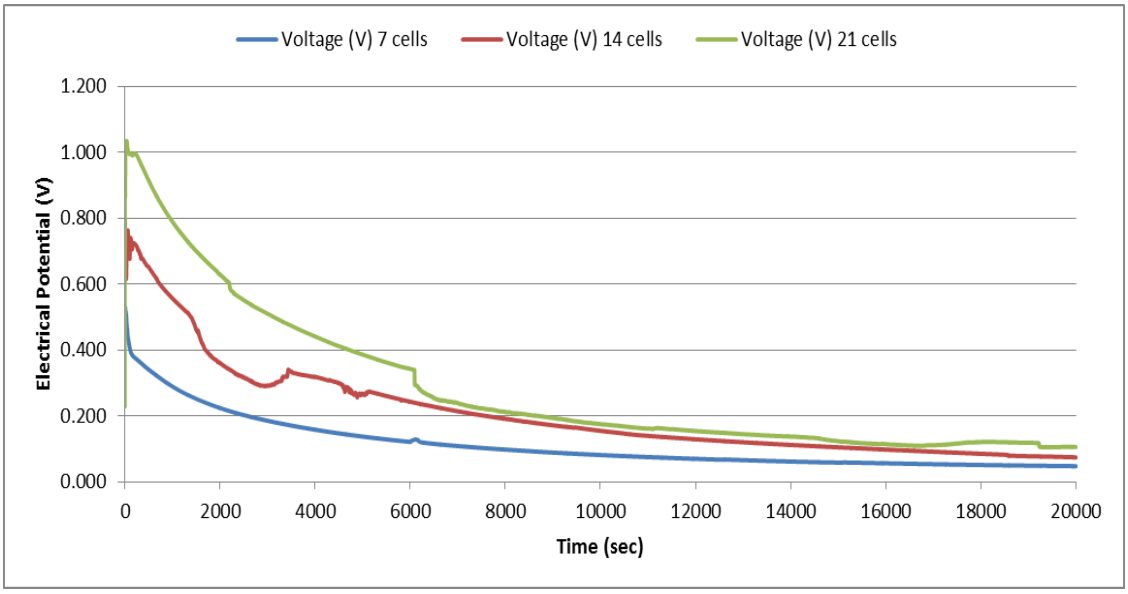

Figure 24 Layout and design of the last iteration before the working prototype.

3.7. Conclusion and Next Steps

In this chapter, a proof of a concept cascaded concentration cells system capable powering small scale implantable pacemaker was demonstrated. In this prototype, the concentration cells were interconnected with fluidic channels, which allowed filling the prototype from a few ports of entry at the cost of reducing the generated voltage and power. Additionally, the internal resistance, efficiency, and power density of the whole system were calculated.

The values for power and power density were calculated from experiments conducted on not fully optimized system. At this point, the system was not fully optimized due to large variations in experimental data that was collected. In order to reduce variations in the collected data, a number of improvements can be made. All handmade processes need be replaced with machine processes. First of all, the filling up process where two syringes filled up with different concentration solutions are used to fill in cells by hand could be replaced with a syringe pump that provides continuous fixed flow rate. Second, during assembly process, a set of thumbscrews are used to sandwich the system together and hold in place. Currently, the set of screws are tightened by hand and not to the same degree. In order to achieve same repeatable tightening a set of spacers can be introduced and used. Third, a switch board with different resistance values could be used to toggle between different loads during each experiment. This way, one can make sure that all parameters are the same

and the resistive load is the only varying parameter. Forth, the thickness of each cast can also be varied and correlated with recorded electrical potentials. These values could provide more information about the experimental error. Additionally, a better way to seal the compartments and reduce leakage would improve repeatability during experiments.

Another way to improve the overall system's output voltage, power and power density is to find and implement a way for the fluidic channels to be sealed after the filling is accomplished. In fact, the generated electrical potential could be improved by up to 49 percent, and the generated power output up to approximately 69 percent by sealing off channels. Please see Table 13 for further details. Such improvement can be accomplished through an implementation of valves. Active microfluidic components based on magnetically modified elastomeric materials could also be used and could help bonding, or sealing the materials since our casts are already made of elastomeric materials [40, 41].

Table 13: Determining level of possible improvement in generated electrical potential and power.

Concentration Ratio	R_{load} (Ohms)	V_{load} (V) with channels	V_{load} (V) without channels	% voltage improvement	% power improvement
1000	10G (open circuit)	1.19	2.34	49.15	---
	1M	1.05	1.87	43.85	68.47
	500k	0.95	1.55	38.71	62.43
100	500k	1.16	1.41	17.73	32.32
10	500k	0.72	0.76	5.26	10.25

The overall results are encouraging; however, further investigation needs to be done in researching the concentration solutions, optimal cell dimensions, low resistance membranes, power densities and continuous solution flow for direct ionic and electric output current with a goal to develop a low resistance system capable of powering small scale implantable devices.

Appendix A

Figures 25-29 show average of three repeated runs. The error bars indicate maximum and minimum values recorded. The data was plotted at every 250 seconds interval.

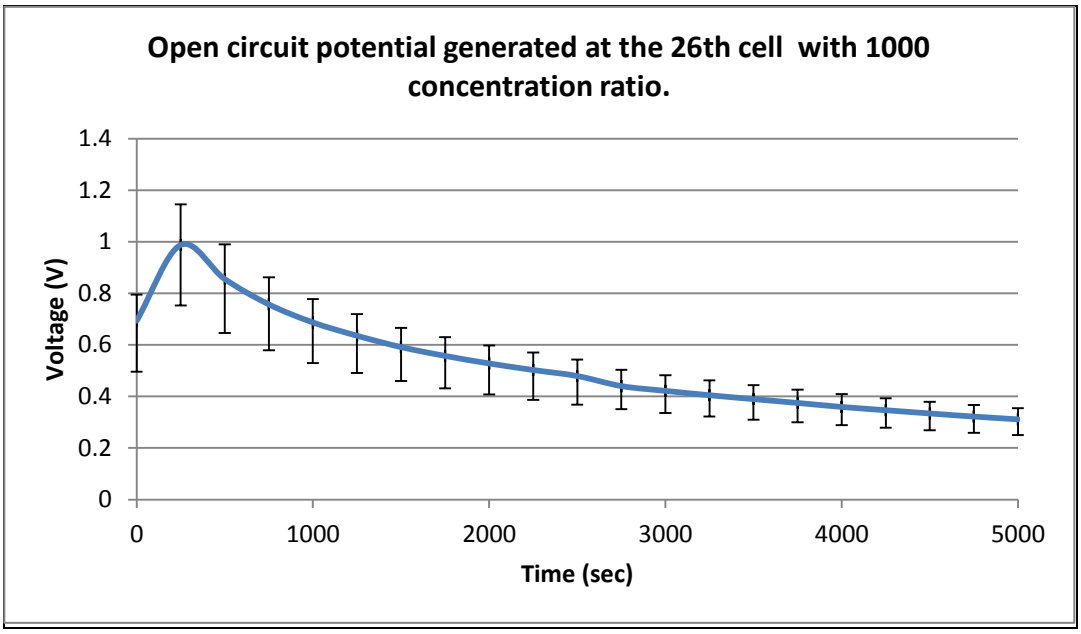

Figure 25: Open circuit potential generated at the 26th cell with 1000 concentration ratio.

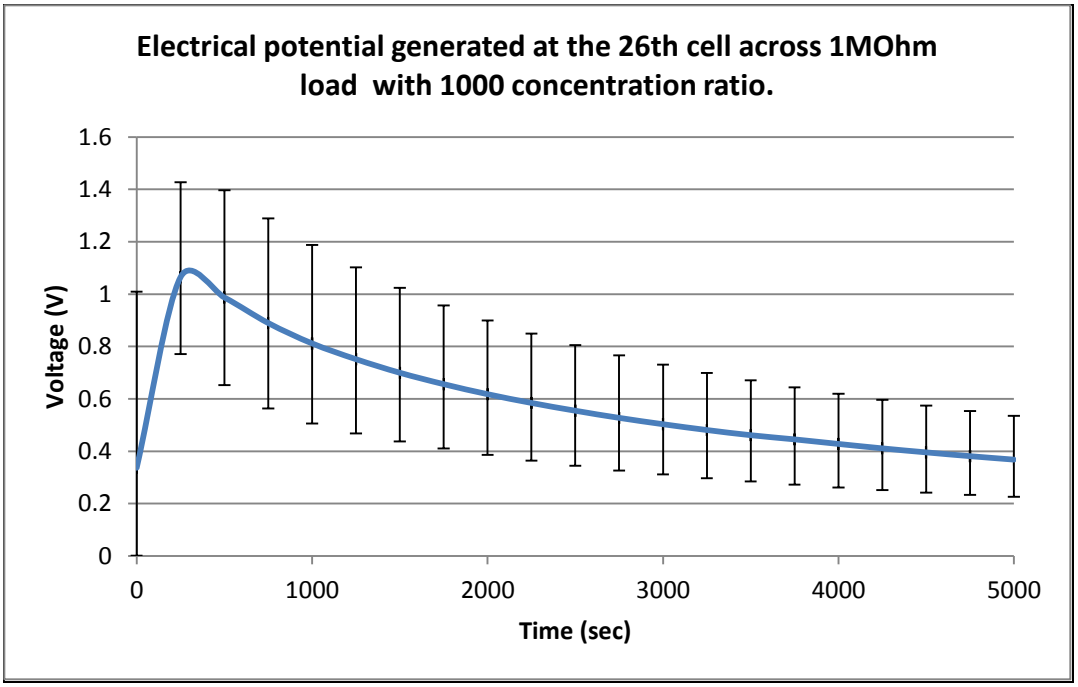

Figure 26: Electrical potential generated at the 26th cell across 1MOhm load with 1000 concentration ratio.

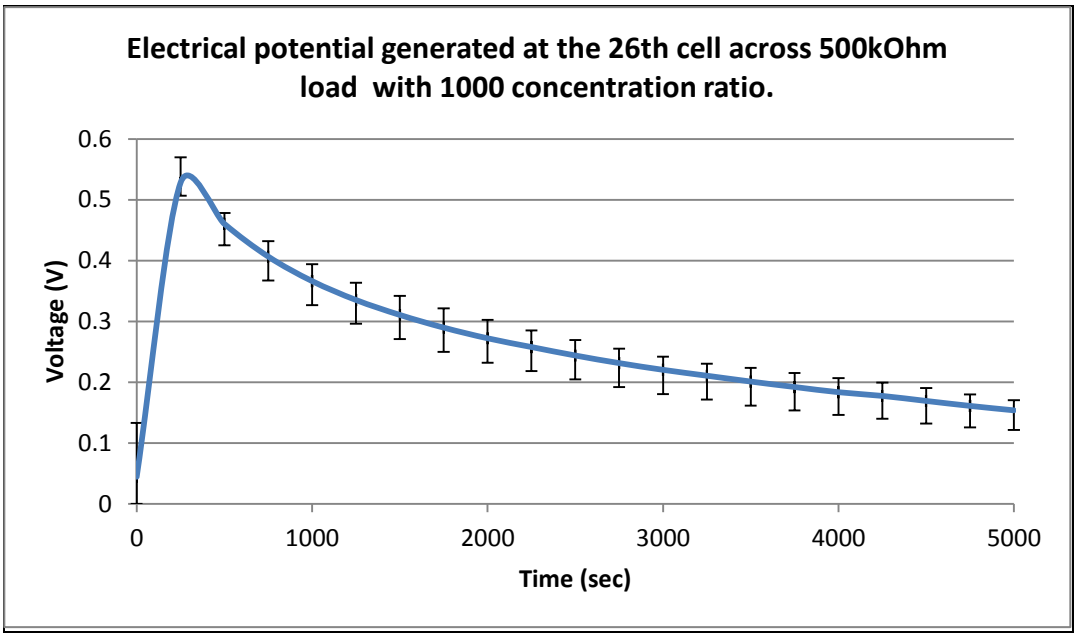

Figure 27: Electrical potential generated at the 26th cell across 500kOhm load with 1000 concentration ratio.

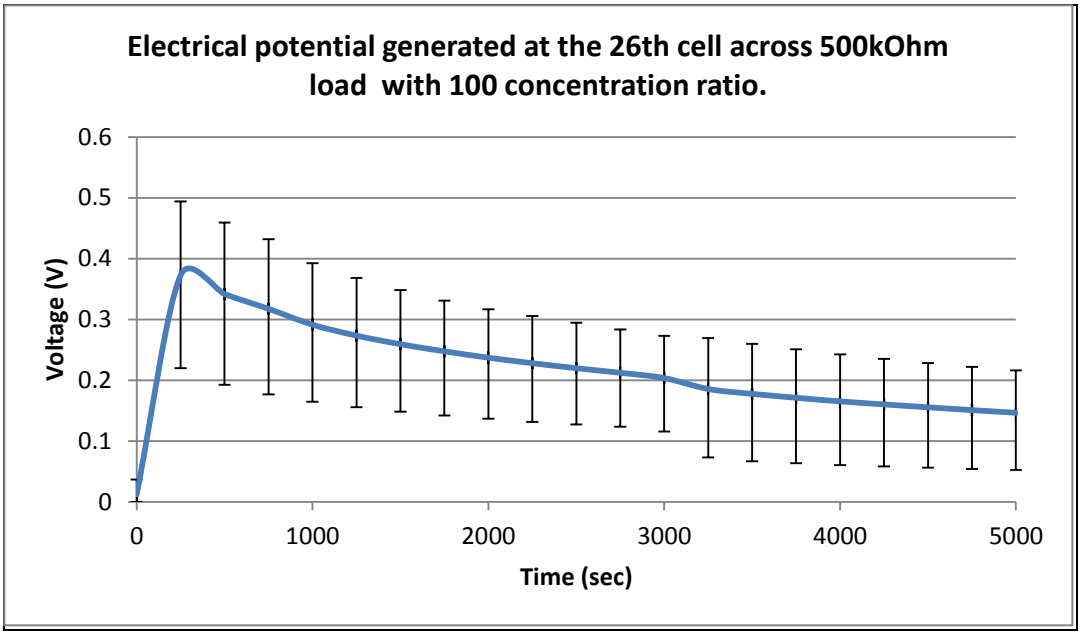

Figure 28: Electrical potential generated at the 26th cell across 500kOhm load with 100 concentration ratio.

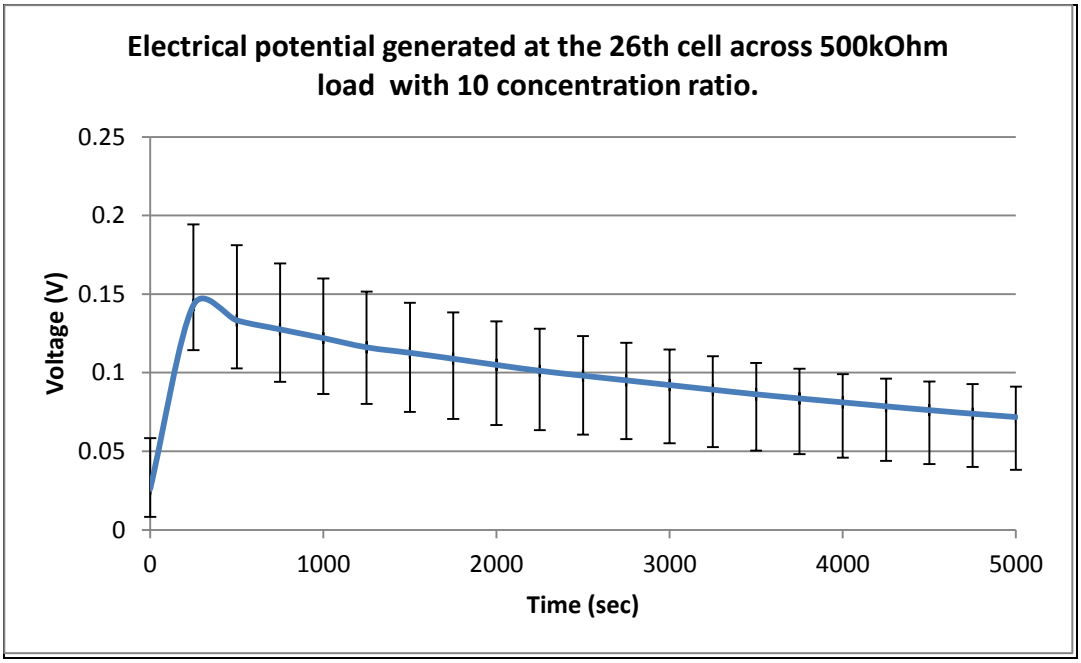

Figure 29: Electrical potential generated at the 26th cell across 500kOhm load with 10 concentration ratio.

Appendix B List of author's publications

1. Pantchenko O, Jackson P, Isaacson M and Shakouri A: **California-Denmark Renewable Energy Summer Program** *American Society for Engineering Education Annual Conference and Exposition*, San Antonio, TX, June 2012.
2. Pantchenko O, Seidman S and Guag J, **Analysis of induced electrical currents from magnetic field coupling inside implantable neurostimulator leads** *BioMedical Engineering OnLine Journal*, Volume 10, Number 94, October 2011.
3. Pantchenko O, Shahab S, Tate D, Matteini P, Isaacson M and Shakouri A: **Work in Progress - Enhancing Students Learning Through Instructional Videos during Hands-On Laboratories on Renewable Energy Sources** *Frontiers in Education Conference*, October 2011.
4. Sadeghian R, Pantchenko O, Tate D and Shakouri A: **Miniaturized concentration cells for small-scale energy harvesting based on reverse electrodialysis** *Applied Physics Letters*, Volume 99, Issue 17, October 2011.
5. Pantchenko O, Seidman S, Guag J, Witters D and Sponbert C: **Electromagnetic compatibility of implantable neurostimulators to RFID emitters** *BioMedical Engineering OnLine Journal*, Volume 10, Number 50, June 2011.
6. Pantchenko O, Tate D, O'Leary D, Isaacson M and Shakouri A: **Enhancing Student Learning through Hands-On Laboratories on Renewable**

Energy Sources *American Society for Engineering Education Annual Conference and Exposition*, June 2011.

7. Pantchenko O, Shavani J, Zebarjadi M **Cascaded Micro Concentration Cells** *UC BioEngineering Symposium*, June 19-21st, 2009, Merced, CA
8. Cockerham K, Aro S, Liu W, Pantchenko O, Olmos A, Oehlerbg M, Sivaprakasam M and Crow L **Application of MEMS technology and engineering in medicine: a new paradigm for facial muscle reanimation** *Expert Review of Medical Devices* 2008 **5**(3) 371-381(11)
9. Work in progress: Pantchenko O, Sadeghian R, Isaacson M, Shakouri A: **A renewable energy power source based on *in vivo* concentration ratios** *Nature*.

Bibliography

1. Krames E: *Neuromodulation*. Oxford, UK, Academic Press, Elsevier Ltd, 2009.
2. Schwalb J, Hamani C: **The History and Future of Deep Brain Stimulation** *Neurotherapeutics: The Journal of the American Society for Experimental NeuroTherapeutics* 2008, **5** 3-13.
3. Gildenberg P: **History of Electrical Neuromodulation for Chronic Pain** *Pain Medicine* 2006, **7** S7-S13.
4. Finkenzeller K: *RFID handbook: fundamentals and applications in contactless smart cards and identification.* Chichester, West Sussex, England, John Wiley & Sons Ltd, 2003.
5. **U.S. Food and Drug Administration: Radiofrequency Identification (RFID)** [http://www.fda.gov/Radiation-EmittingProducts/RadiationSafety/ElectromagneticCompatibilityEMC/ucm116647.htm.]
6. **U.S. Food and Drug Administration: Radiofrequency Identification Technology: Protecting the Drug Supply** **[**http://www.fda.gov/Drugs/DrugSafety/ucm169918.htm]
7. Roberti M: **RFID in Health Care West**. RFID Journal; 2010 Jun 15, Los Angeles, CA, USA.
8. **Retained Surgical Items** [http://nothingleftbehind.org]

9. Christe B, Rogers R, Cooney E: **Analysis of the Impact of a Radiofrequency Identification Asset-Tracking System in the Healthcare Setting** *Journal of Clinical Engineering* 2010, **35**(1) 49-55
10. van der Togt R, van Lieshout E, Hensbroek R, Beinat E, Binnekade J, Bakker P: **Electromagnetic interference from radio frequency identification inducing potentially hazardous incidents in critical care medical equipment** *JAMA 2008,* **299**(24) 2884-90
11. Seidman S, Brockman R, Lewis B, Guag J, Shein M, Clement W, Kippola J, Digby D, Barber C, Huntwork D: **In vitro tests reveal sample radiofrequency identification readers inducing clinically significant electromagnetic interference to implantable pacemakers and implantable cardioverter-defibrillators** *Heart Rhythm* 2009, **7**(1) 99-107
12. Dustin K: **Evaluation of Electromagnetic Incompatibility Concerns for Deep Brain Stimulators** *Journal of Neuroscience Nursing* 2008, **40**(5) 299-319
13. Kainz W, Neubauer G, Alesch F, Schmid G, Jahn O: **Review of the Literature: Electromagnetic compatibility of electronic implants** *Wiener Klinische Wochenschrift* 2001, **113**(23-24) 903-14
14. **U. S. Food and Drug Administration, Important Information on Anti-Theft and Medical Detector Systems and Pacemakers, ICDs, and Spinal Cord Stimulators**

[http://www.fda.gov/MedicalDevices/Safety/AlertsandNotices/PublicHealthNotifications/UCM062288]

15. **ANSI/AAMI/ISO 14708-3 2008 American National Standard for Implants for Surgery – Active implantable Medical Devices – Part 3: Implantable Neurostimulators**
16. Pantchenko O, Seidman S, Guag J, Witters D, Sponberg C: **Electromagnetic compatibility of implantable neurostimulators to RFID emitters** *BioMedical Engineering Online* 2011, **10**:50.
17. Hrdlicka G: **Implantable Neurostimulator and the EMC Environment** *IEEE International Symposium on Electromagnetic Compatibility* 2002, vol. 2, 916-919.
18. Bassen H I, Mendoza G G: **In-Vitro mapping of E-fields induced near pacemaker leads by simulated MR gradient fields** *BioMedical Engineering OnLine* 2009, **8**:39.
19. Ulaby F: *Fundamentals of Applied Electromagnetics* Prentice Hall, 2004.
20. **Speag, Eli** [http://www.speag.com/products/dasy/sar-phantoms/eli/]
21. Reilly J P, Diamant A M: *Electrostimulation: Theory, Applications, and Computational Model.* Artech House, 2011.
22. Abejon D, Cameron T, Feler C, Perez-Cajaraville J: **Electric Parameters Optimization in Spinal Cord Stimulation. Study in Conventional Nonrechargeable Systems** *Neuromodulation* 2010, **13** 281-287.

23. Struijk J, Holsheimer J, van der Heide G, Boom H: **Recruitment of Dorsal Column Fibers in Spinal Cord Stimulation: Influence of Collateral Branching** *IEEE Transactions on Biomedical Engineering* 1992, **39** (9) 903-912.

24. Holsheimer J, Wesselink W: **Optimum Electrode Geometry for Spinal Cord Stimulation: the narrow bipole and tripole** *Med. Biol. Eng. Comput.* 1997, **35** 493-497.

25. Reilly J: *Applied Bioelectricity: From Electrical Stimulation to Electropathology*. Springer-Verlag, New York, 1998.

26. Barton S, Gallaway J, Atanassov P: **Enzymatic Biofuel Cells for Implantable and Microscale Devices** *Chem. Rev*. 2004, 104 4867-4886.

27. Parsonnet V, Driller J, Cook D, Rizvi S: **Thirty one year of clinical experience with "nuclear-powered" pacemakers.** *Pacing Clinical Electrophysiology* 2006, 29(2) 195 -200.

28. Weijand K: **Body Heat Power Implantable Medical Device**, US Patent 6470212, 2002.

29. Lewandowski B, Kilgore K, Gustafson K: **Design Considerations for an Implantable, Muscle Powered Piezoelectric System for Generating Electrical Power** *Annals of Biomedical Engineering* 2007 **35(4)** 631-641.

30. Algora C, Pena R: **Recharging the battery of implantable biomedical devices by light** 2009 *Artif. Organs.* 33(10) 855-860.

31. Linford R, Latham R, Schlindwein W: **Biomedical Applications of Batteries**, *Solid State Ionics*, 2004 **172(1-4)** 7-11.

32. Soykan O: **Power Sources for Implantable Medical Devices** *Business Briefing: Medical Device Manufacturing & Technology* 2002.

33. Xu J, Lavan D: **Designing artificial cells to harness the biological ion concentration gradient** 2008 *Nature Nanotechnology* doi:10.1038/nnano.2008.274.

34. Sadeghian R, Pantchenko O, Tate D, Shakouri A: **Miniaturized concentration cells for small scale energy harvesting based on reverse electrodialysis** 2011 *Applied Physics Letters* ***99(17).***

35. Bard A, Faulkner L: *Electrochemical Methods: Fundamentals and Applications.* Second Edition. John Wiley & Sons, Inc. 2001.

36. Veerman J, Saakes M, Metz S, Harmsen G: **Reverse electrodialysis: Performance of a stack with 50 cells on the mixing of sea and river water** *Journal of Membrane Science* 2009 **327** 136-144.

37. Dluglecki P, Nymeijer K, Metz S, Wessling M: **Current status of ion exchange membranes for power generation from salinity gradients** 2008 *Journal of Membrane Science* 2008 **319** 214-222.

38. Fumasep FAD, Technical Data Sheet http://www.fumatech.com/NR/rdonlyres/C90FFA61-9F34-4D21-9C8A-9BF3020F227D/0/fumasepFAD.pdf

39. Sadeghian R Personal Communication September 13, 2011.

40. Pamme N: **Magnetism and Microfluidics** *Lab Chip* 2006 **6** 24-38.

41. Jackson W, Tran H, O'Brien M, Rabinovich E, Lopez G: **Rapid prototyping of active microfluidic components based on magnetically modified elastomeric materials** 2001 *J. Vac. Sci. Technol. B* **19**(2) 596-599.